Soft X-ray fluxes as a diagnostic for hot plasmas

P. Smeulders

IPP 2/233 Januar 1979

MAX-PLANCK-INSTITUT FÜR PLASMAPHYSIK

8046 GARCHING BEI MÜNCHEN

MAX-PLANCK-INSTITUT FÜR PLASMAPHYSIK

GARCHING BEI MÜNCHEN

Soft X-ray fluxes as a diagnostic for hot plasmas

P. Smeulders

IPP 2/233 Januar 1979

Die nachstehende Arbeit wurde im Rahmen des Vertrages zwischen dem Max-Planck-Institut für Plasmaphysik und der Europäischen Atomgemeinschaft über die Zusammenarbeit auf dem Gebiete der Plasmaphysik durchgeführt.

IPP 2/233 P. Smeulders

Soft X-ray fluxes as a diagnostic for hot plasmas.

January 1979

Abstract

The continuous emission spectrum through different absorbers is calculated for given impurity distributions. The coronal equilibrium has mainly been used. Estimates based on finite life time effects are given for departures from the coronal equilibrium. In particular, the effects of the molybdenum L-line radiation and of the radial profiles are studied.

Graphs and tables allow analytic corrections to be made. In the case of the W VII A Stellarator good agreement with other electron temperature and Z_{eff} measurements has been found.

Content

1. Introduction

The determination of plasma parameters by X-ray analysis is already a long established technique /3/. With increasing plasma temperatures and observed internal instabilities in the hot central region of an ohmically heated plasma the X-ray diagnosis has however gained increasing interest. Especially, since the instabilities contribute for a large part to the limitation of the energy life time of the electrons. The calculation in this paper of the continuum radiation has been published previously /1/, but here we will go into more detail about the problems associated with the emission and the integration of it along the line of sight.

In contrast to measurements in the UV or VUV in present size plasmas, fluxes in X-ray spectrometers are relatively small. In Si(Li)-spectrometers fluxes are restricted due to pulse pile-up problems at higher count rates and in crystal spectrographs the incident beam is restricted to a small solid angle.

It is therefore convenient to use detectors which integrate the spectrum over a certain energy domain. The fluxes can thus be made large enough that fast changes of plasma parameters become noticeable on the measured X-ray fluxes. (The m = o, n = o sawtooth and m = 1, n = 1 and other modes /11, 13, 15/.) In most cases, by a suitable choice of filter and detector type and thickness, one can eliminate the line emission part of the spectrum. Such a choice must be verified by spectrum measurements /1/. This will be shown later for Wendelstein VII A measurements. It is then possible to interpretate the signals by calculations of the continuum emission only. Compared with the often complex nature /7, 8, 11/ of the multi-line emission in certain energy domains this simplifies the analysis.

The required knowledge about the type of impurity and its ionization stage may be obtained either from theoretical arguments or from spectroscopic observations in the VUV and soft X-ray region.

We will restrict ourselves to thermal continua only; so the so-called slide-away /14/ and runaway regimes at lower electron densities ($n_e \lesssim 10^{13}$ particles per cc) will not be considered in this paper.

2. The continuum spectrum for a homogeneous plasma

2.1. The hydrogenic ion

The emission spectrum for a Maxwellian plasma and a hydrogenic ion is well known /4b/ and is given by

$$P(h\nu) = 2.4\,10^{-16}\, n_e n_z Z^2 T_e^{-1/2} \left\{ \langle g_{ff} \rangle + \sum_{n=1}^{\infty} g_{fb}(n) \cdot \frac{2 Z^2 I_H}{n^3 T_e} \cdot \exp\left(\frac{Z^2 I_H}{n^2 T_e}\right) \right\} \cdot \exp\left(-\frac{h\nu}{T_e}\right) \qquad (1)$$

$P(h\nu)$ in $(cm^3 \cdot ster \cdot sec)^{-1}$

n_e, n_z : electron and ion densities in cm^{-3}

T_e : electron temperature in keV

n : principal quantum number for the recombination radiation

$\langle g_{ff} \rangle$, $g_{fb}(n)$: the Gaunt factors for the free-free and the free-bound radiation /4b/

I_H : ionization energy of hydrogen: 0.0136 keV

$h\nu$: X-ray energy in keV

2.2. The non-hydrogen ion

For a non-hydrogen ion the continuous emission cannot be calculated exactly /4c/. Various simplified solutions have been proposed in the past /7, 9/ in order to take into account the screening of the nucleonic charge by the bounded electrons. One solution is to take an effective quantum number $n^+ = n - \mu$, n = quantum number, μ: quantum defect /9/ as is shown in a review article by Mattioli, $n^+ = \sqrt{Z^2 I_n / E_i}$, E_i = ionization energy of the ion with charge Z + 1; n^+ then replaces, in the hydrogenic free-bound equation, the quantum number of the first electron shell which is not completely occupied. Radiative recombinations to higher levels are then usually taken to be hydrogenic (without n^+).

A second solution is to take an effective ion charge Z^*, as indicated in the review article of Bambynek /10/, $Z^* = \sqrt{n_0^2 E_i / I_H}$, where n_0 = the quantum number of the shell, which is the first to be partially (or not) occupied. Z^* is always larger than Z since the screening is incomplete, $Z^* = Z_N - \sigma$, σ : screening constant, Z_N: nucleonic charge. In the calculations mentioned in this paper as previously /1, 2/, the Z^* is taken for recombination to all quantum levels (n), for the following reason.

For a given X-ray energy $h\nu$ the initial electron energy before recombination has to increase when we increase the quantum level n. Hence, the encounter electron-nucleus will have to be closer and the effectiveness of the screening by the peripheral electrons will decrease. This is a similar argument as used for the free-free radiation /4c/. So the second mentioned solution where Z^* is taken for all quantum levels, will be more accurate than the first solution where n^+ is taken for the non-fully occupied lowest quantum level only /7/. Apart from this there is no significant difference between the use of the quantum defect or the screening constant.

These methods are certainly not exact. So extensive calculations, like those which have been performed /12/ for the line emission processes, are useful in order to check the approximation used above. The error introduced in the effective plasma charge Z_{eff} for lower values of it is however not large, since at lower electron temperatures, $T_e \sim 300$ eV, the dependence of the X-ray intensity on the impurity concentration is quite strong; especially for the light impurities (oxygen for example). This reduces the requirements on the accuracy of the calculation. At higher temperatures ($T_e \sim 2000$ eV) even medium weight impurities (like iron) are highly ionized and thus hydrogen-like, so that the approximation of the screening of the nucleus is accurate.

The free-bound emission can be seen as a limiting case of the bound-bound emission. Cowan /12/ estimates the accuracy of the hydrogenic approximation in the case for $\Delta n > 1$ to better than 40%. So that it is expected that the uncertainty due to the screening of the nucleus will be well within that caused by the unknown chemical composition (discussed later for Fig.2).

2.3. The Gaunt factors

The quantum mechanical corrections for the classical free-free and free-bound emission formulas or the Gaunt factors /4b/ are included in the calculations. When possible the approximations given in /4a/ are used in order to reduce computation time.

For the same reason an additional approximation is used: namely for $\xi \geq 3$ and $\eta \geq 1$; ξ and η have the same meanings as in /4a/ and are

$$\xi = \eta' - \eta \quad ; \quad \eta = \sqrt{\frac{Z^2 I_H}{E_i}} \quad ; \quad \eta' = \sqrt{\frac{Z^2 I_H}{E_f}}$$

η is the modified quantum number and equals the de Broglie wavelength over the minimum impact parameter of the free electron.

E_i and E_f are the initial and final energy of the electron with $h\nu = E_i - E_f$:

$$g_{ff} = \frac{\sqrt{3}}{\pi} \cdot \left(1 + 0.548\, {}^{10}\log\left(\frac{E_i}{h\nu}\right) \eta^{-0.557}\right) \cdot \left(1 + 0.1728\, \eta^{-2/3} - 0.0496\, \eta^{-4/3} - 0.0172\, \eta^{-6/3} + \ldots\right) \qquad (2)$$

This relation is found numerically from the Menzel-Pekeris formula with the aid of formula (6) of /4a/. The maximum error is the same as mentioned for formula (6) $\leq$ .2%. Otherwise the Menzel-Pekeris formula is used. For the free-bound calculations the tables given in /4b/ are taken.

2.4. The relativistic correction

As is shown in /1/ for present-day ohmically heated plasmas with $T_e < 3$ keV it is not necessary to include relativistic effects. For future reactor plasmas with $T_e \backsim 20$ keV the calculations should, however, include a relativistic correction.

2.5. The total continuum emission

The total emission can be expressed as follows:

$$P(h\nu) = \sum_i 2.4\, 10^{-16}\, n_e\, n_i\, Z_i^{*2}\, T_e^{-1/2} \left(\langle C_{rel}\, g_{ff} \rangle + \sum_{n=n_o}^{\infty} C_{rel}\, g_{fb}(n)\, \frac{\mu\, Z_i^{*2}\, I_H}{n^3\, T_e} \cdot \exp\left(\frac{Z_i^{*2}\, I_H}{n^2\, T_e}\right) \right) \exp\left(-\frac{h\nu}{T_e}\right) \qquad (3)$$

with P in $cm^{-3}\ ster^{-1}\ sec^{-1}$.

n_i = ion density in cm^{-3}

$Z_i^{*2} = \frac{n_o^2\, E_i}{I_H}$

n, n_o = quantum number and lowest quantum number for recombination radiation

μ = number of free places in the n^{th} electron shell divided by n^2 /9/

$\langle C_{rel}\, g_{ff} \rangle$ = relativistic correction factor times the free-free Gaunt factor averaged over a Maxwellian electron velocity distribution

$g_{fb}(n)$ = free-bound Gaunt factor

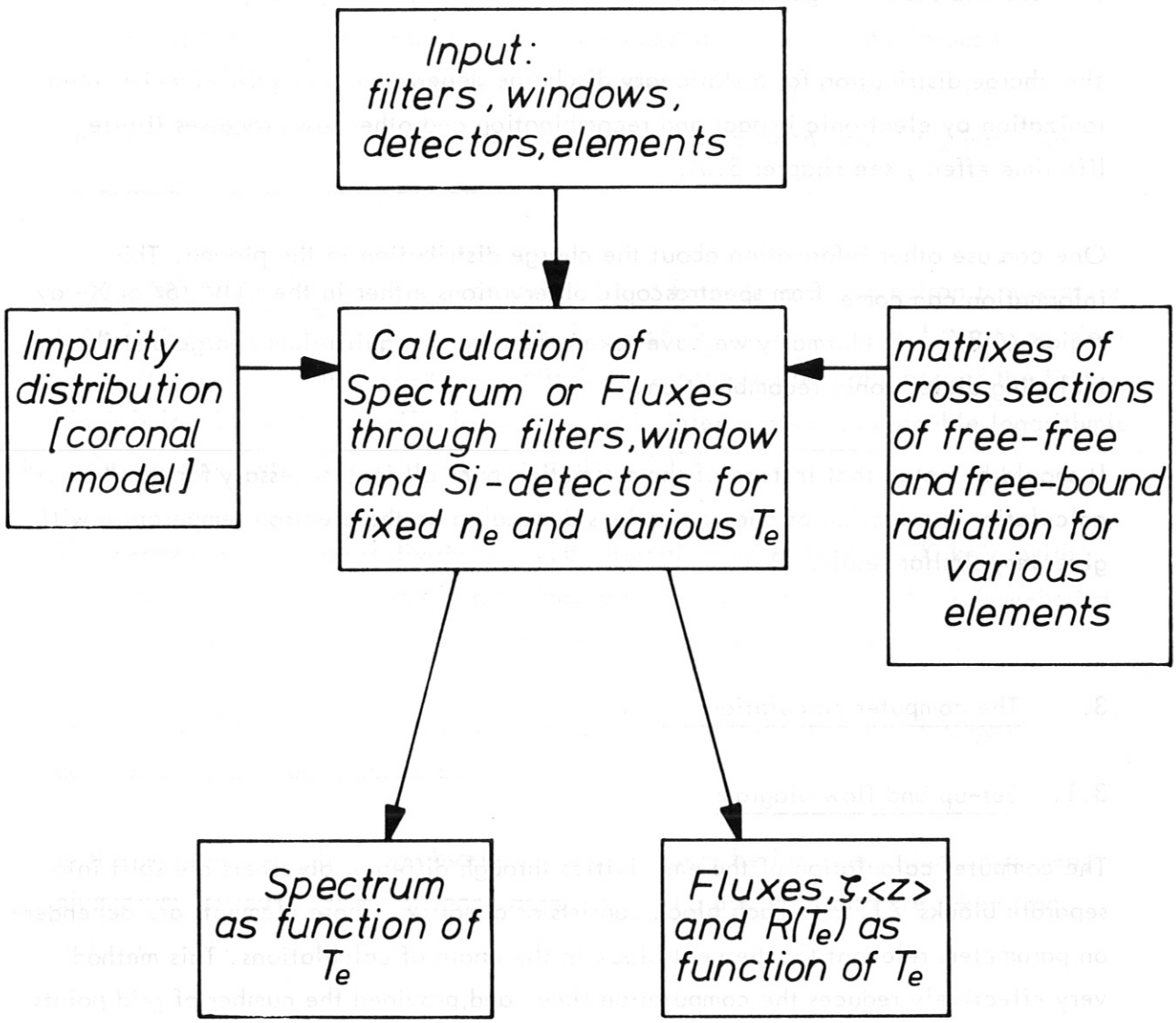

Fig. 1 Flow diagram of the computations of the X-ray continuum emission.

The computer calculation of the above equation is described in /1/ and /2/ and covers the following electron temperature range: T_e: from 45 eV to 4000 eV. The electron density is arbitrary and is taken $5 \cdot 10^{13} cm^{-3}$.

The ions and their charge distribution are calculated separately /20/.

The charge distribution for a stationary discharge depends on an equilibrium between ionization by electronic impact and recombination and other loss processes (finite life time effect, see chapter 3.3).

One can use other information about the charge distribution in the plasma. This information can come from spectroscopic observations either in the VUV /6/ or X-ray region /13/ Normally we have taken the coronal equilibrium charge distribution including dielectronic recombination.

It should be noted that instead of the summation over all ions necessary for the "exact" calculation, a selection of one or two ions depending on the electron temperature will give very similar results /1/.

3. The computer calculations

3.1. Set-up and flow diagram

The computer calculation of the emissivities through different absorbers are split into separate blocks /1, 2/. Each block consists of a matrix, whose elements are dependent on parameters relevant for the next block in the chain of calculations. This method very effectively reduces the computation time and, provided the number of grid points for each parameter is sufficiently large, the accuracy is not sacrified ($\leq 10^{-3}$). With reference to the flow diagram of Fig.1: the first block calculates the free-free and the free-bound cross sections /4a, 4b, 4c/ as a function of the electron temperature T_e and of the X-ray energy $h\nu$. The free-free matrix has a 5 x 6 double-log grid spacing for T_e and $h\nu$ defined by $T_e = 13.6 \quad 10^{I/2}$ where I equals 1 to 5 and $h\nu = 13.6 \quad 10^{J/2}$ where J is 1 to 6. The free-bound matrix has also a double-log grid with $T_e = 13.6 \quad 10^{(I+1)/4}$ with I = 1,9. $h\nu$ has a total of 19 points with at least three points in between the free-bound discontinuities. This first block is then calculated for each type of ion with an effective nucleonic charge Z^* calculated

from the binding energies obtained from W.Lotz /16/ and J.L.Schwob /17/. In the examples given below four groups of blocks are calculated for hydrogen, helium, oxygen and iron, respectively.

In this paper we will only concentrate on these four groups, since the results concerning the shape of the spectrum and the absolute value of the intensity for Molybdenum are calculated to be within those for oxygen and iron. In addition, for the W VII A experiments oxygen is the dominant impurity, with iron the second most important /21, 23/.

In the next block the spectrum is calculated as a function of the electron temperature with $T_e = 10^{(I/10 - 1.4)}$ $I = 1, \ldots, 20$. For each T_e and hν value the cross sections of the free-free and the free-bound radiation are obtained from the part of the first block belonging to the specific ion by quadratic interpolation on a double logarithmic scale. This has an estimated accuracy of about 10^{-3}.

The X-ray energy range is divided into 28 intervals from 400 eV to 100 keV, with the boundaries of the intervals corresponding to the discontinuities of the free-bound emission of the ion and to the discontinuities of the absorbers concerned.

Then the number of grid points in each interval is determined such that a good quadratic integration is possible.

In the program the following absorbers can be chosen: helium, beryllium, nitrogen, aluminium, silicon, gold, oxygen, argon, air. The absorber data are taken from Veigele /5/.

Next the data for the charge distribution of each element (H, He, O, Fe) are taken from a separate block /19,20/. In this way the two intensities and their ratio, which pass through two absorbers and fall upon the detectors, are calculated as a function of the electron temperature.

In addition, the enhancement ξ of the radiation over that of pure hydrogen is calculated as well as the average charges $\overline{Z}$ and $\overline{Z^2}$ of the element.

3.2. The results for helium, oxygen and iron continua

In this chapter the relation between the calculated intensities and the effective charge of the plasma Z_{eff} will be derived. This relation is used in section (6.3).

3.2.1. Hydrogen with only one impurity

The intensity of the X-ray radiation emitted from a hydrogen plasma with only one impurity can be written as

$$I = n_H / n_e \cdot I_H + n_z / n_e \cdot \overline{Z} \cdot I_z \qquad (4)$$

with n_e, n_H, n_z the electron, hydrogen and impurity concentration, respectively.

I_H and I_z are calculated by the program for each element concerned.

We write n_H/n_e as p_H and n_z/n_e as p_z, I/I_H as ζ and I_z/I_H as ζ_z.

We recall that

$$n_e Z_{eff} = n_H + n_z \cdot Z^2 \qquad (5)$$

and

$$n_e = n_H + n_z \cdot Z \qquad (6)$$

where the averaged charges $\overline{Z^2} = \sum_i f_i Z_i^2$ and $\overline{Z} = \sum_i f_i Z_i$ for each element are obtained from the relative charge distribution f_i as usual.

The equations (4), (5) and (6) lead to

$$\zeta = p_H + p_z \overline{Z} \zeta_z \qquad (7)$$

$$Z_{eff} = p_H + p_z \overline{Z^2} \qquad (8)$$

$$1 = p_H + p_z \overline{Z} \qquad (9)$$

from which a simple relationship between the measured ζ and the Z_{eff} can be obtained:

$$\Delta Z_{eff} = Z_{eff} - 1 = \frac{\langle Z \rangle - 1}{\zeta_z - 1} \times (\zeta - 1) \qquad (10)$$

with $\langle Z \rangle = \overline{Z^2}/\overline{Z}$.

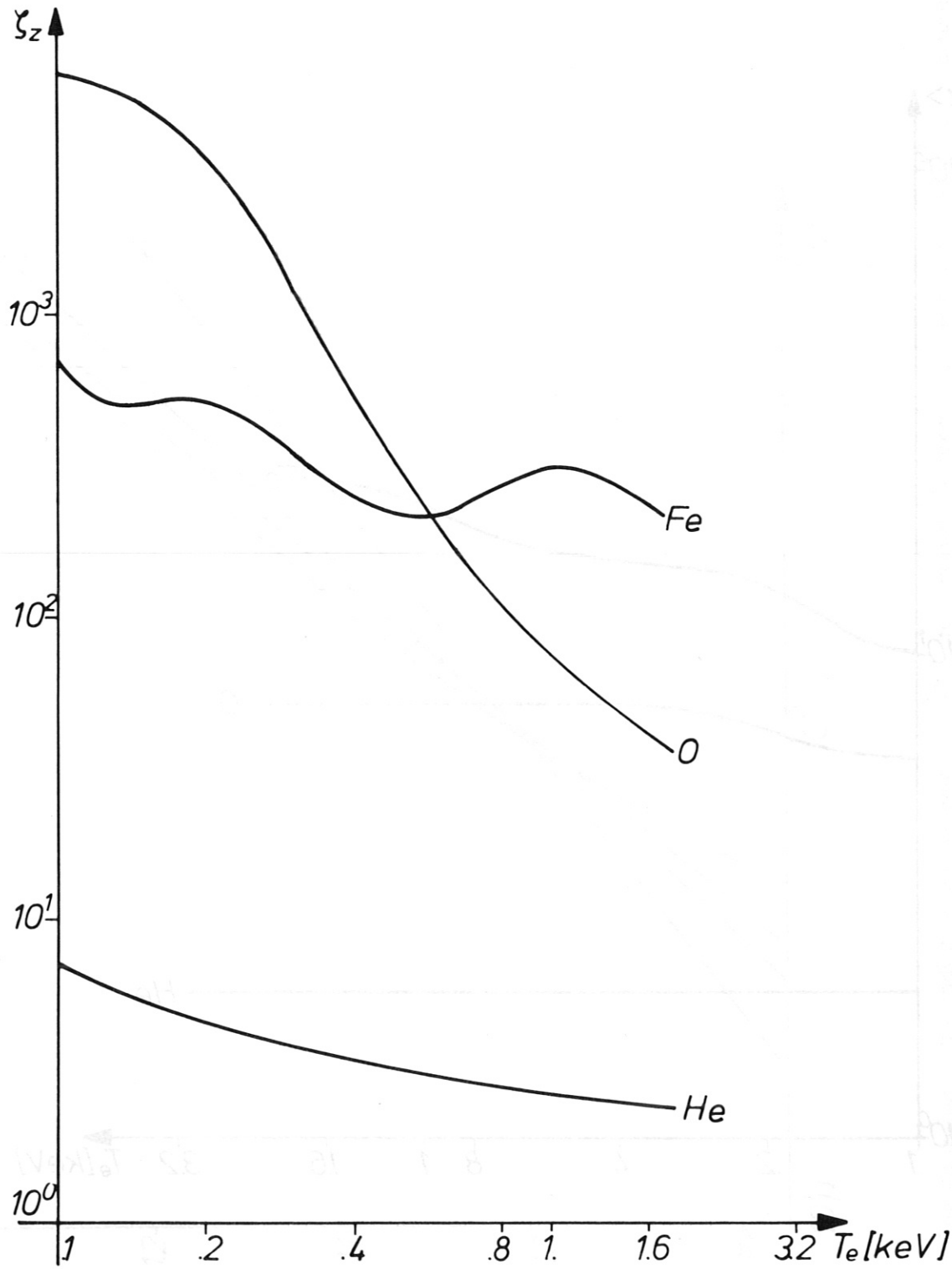

Fig.2 The enhancement ζ_z of the continuum radiation over that for hydrogen as a function of the electron temperature T_e for helium, oxygen and iron through a 738 μ thick beryllium filter.

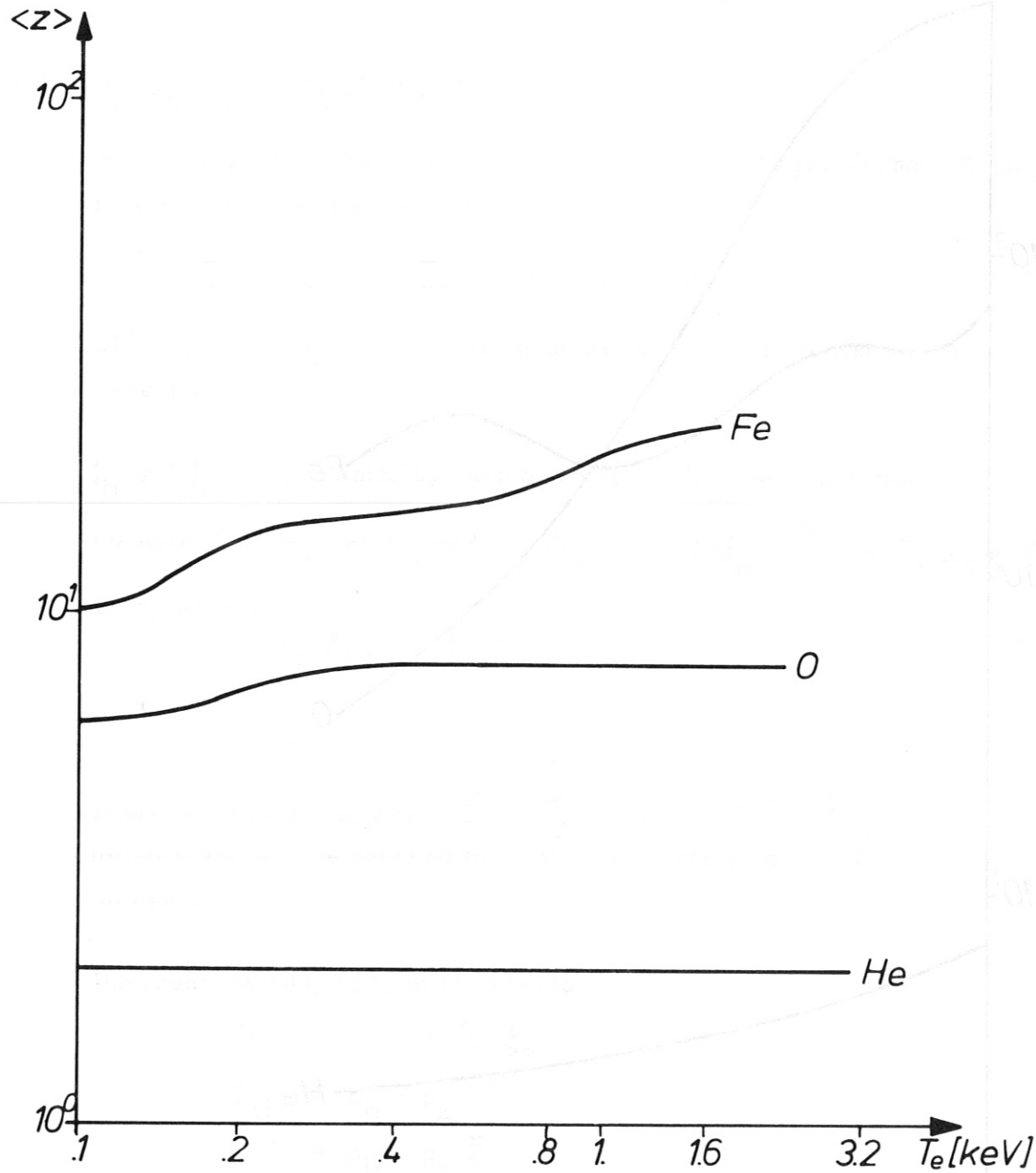

Fig.3 The averaged ionic charge $\langle Z \rangle$ for various elements in coronal equilibrium as a function of the electron temperature T_e.

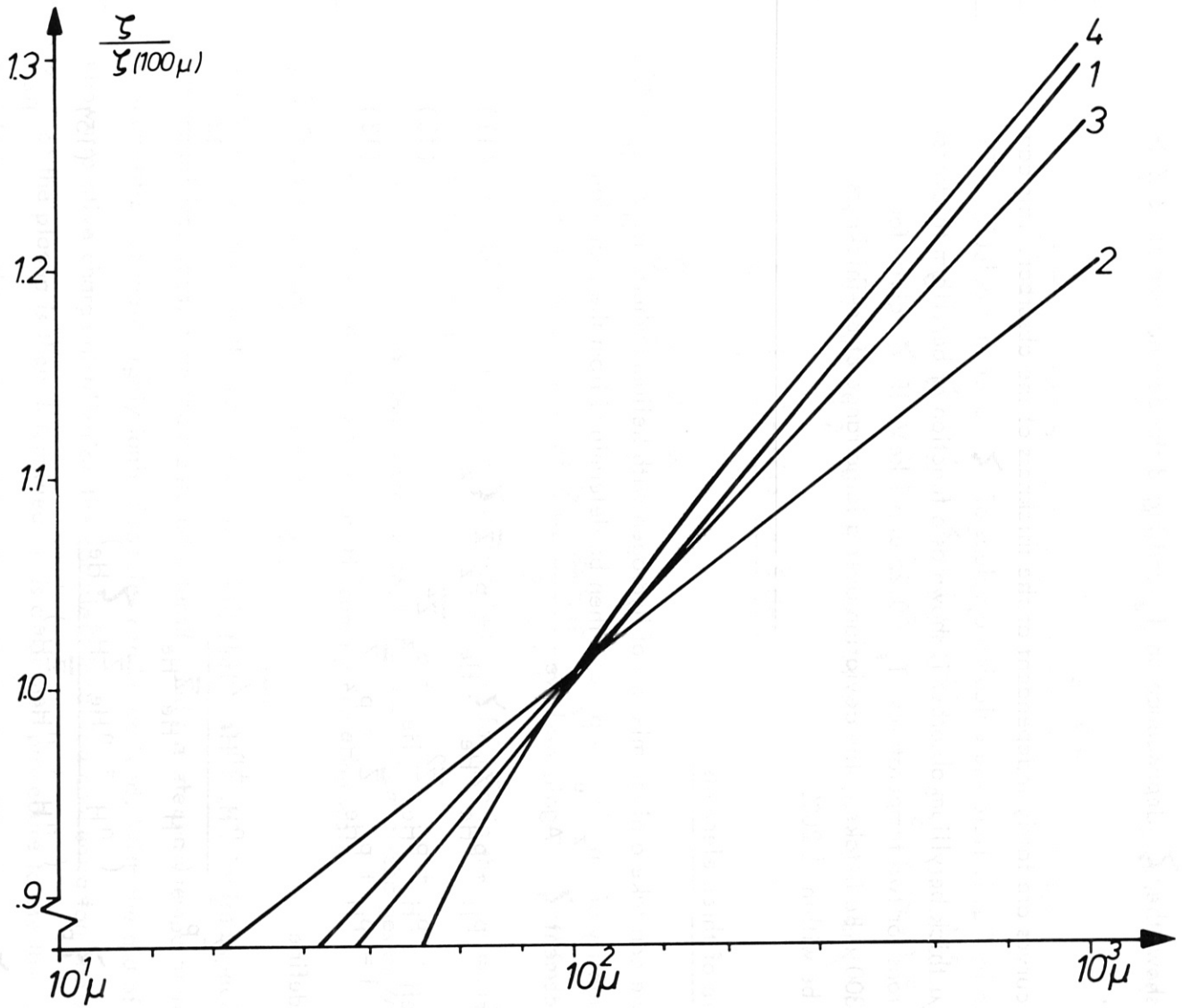

Fig.4 The variation of the radiation enhancement ζ for various elements and electron temperatures as a function of the beryllium thickness.

(1 : oxygen at 0.25 keV; 3 : iron at 0.25 keV;
2 : oxygen at 1.00 keV; 4 : iron at 1.00 keV)

ζ_z and $\langle Z \rangle$ are given by the program for each element as a function of the electron temperature T_e. Examples for a detection system consisting of 738 μ beryllium, 1.75 cm helium, 200 Å gold and 0.2 μ silicon absorbers and a 500 μ thick silicon detector are given in Figs.2 and 3 for helium, oxygen and iron, respectively.

Fig.2 shows the ζ dependence on T_e and Fig.3 the dependence of $\langle Z \rangle$ on T_e.

These curves are fairly independent of the thickness of the absorber. This can be seen in Fig.4. Here the calculated values of ζ over that calculated for a 100 μ thick beryllium absorber is shown as a function of beryllium thickness in microns for two temperatures: T_e = 0.25 and 1 keV. If ζ given for d = 300 μ Be is taken, the deviation over a large range of Be-thickness would be within $\pm$ 20%.

3.2.2. Mixture of three elements

Here we can take a given mixture of hydrogen with helium, where $n_H/n_{He} = \alpha$. The quantity of $n_z/n_e = p_z$ can then be determined from the radiation enhancement ζ. Again we have

$$\zeta = p_H + p_{He}\ \bar{Z}_{He}\ \zeta_{He} + p_z\ \bar{Z}\ \zeta_z \qquad (11)$$

$$Z_{eff} = p_H + p_{He}\ \bar{Z}^2_{He} + p_z\ \bar{Z}^2 \qquad (12)$$

$$1 = p_H + p_{He}\ \bar{Z}_{He} + p_z\ \bar{Z} \qquad (13)$$

If we define

$$Z_p = \frac{n_H + n_{He}\ \bar{Z}^2_{He})}{(n_H + n_{He}\ \bar{Z}_{He})} \qquad (14)$$

and

$$\zeta_p = \frac{(n_H + n_{He}\ \bar{Z}_{He}\ \zeta_{He})}{(n_H + n_{He}\ \bar{Z}_{He})} \qquad (15)$$

Z_p and ζ_p are the primary effective charge and radiation enhancement, without the other third element being present. We get the enhancement of effective plasma ionic charge: ΔZ_{eff}

$$\Delta Z_{eff} = (\langle Z \rangle - Z_p) \cdot \frac{\zeta - \zeta_p}{\zeta_z - \zeta_p} \qquad (16)$$

It can readily be seen that any other element instead of helium could have been taken provided that the relative concentration is known.

In the particular case of an helium - hydrogen mixture approximations can be used giving an expression for ΔZ_{eff} almost independent of $\alpha = n_H / n_{He}$:

$$\Delta Z_{eff} = (\langle Z \rangle - 1.5) \cdot \frac{\zeta - 3/4\ \zeta_{He}}{\zeta_z - 3/4\ \zeta_{He}} \quad (1 + \varepsilon) \qquad (17)$$

$$\varepsilon = \delta_1 \cdot \frac{9}{8} \frac{\zeta_{He} (\zeta_z - \zeta)}{\zeta\ \zeta_z} - \delta_2 \frac{1.5}{\langle Z \rangle - 1.5} \qquad (18)$$

with δ_1 and δ_2 obtained with aid of equations (14) and (15)

$$\delta_1 = \frac{1}{3} \frac{2 - \alpha(3 - 4/\zeta_{He})}{2 +} \qquad (19)$$

$$\delta_2 = \frac{1}{3} \frac{2 - \alpha}{2 + \alpha} \qquad (20)$$

With practical values of $\zeta \backsim \frac{\Delta Z_{eff}}{Z - 1.5}$, ε can be estimated to be $|\varepsilon| \leq 15\%$ for oxygen and slightly better for iron in the temperature range indicated in Fig.2.

Equation (17) is used in section (6.3) for the Helium discharges of W VII-A, which always contain an amount of H coming from the wall.

3.3 Departures from coronal equilibrium

The X-ray emission in the continuum is mainly due to the highly ionised specie s of the impurities. Thus, from the measured intensity and the electron temperature the concentration of these highly ionised species can be derived. With the aid of a known relative charge distribution the complete local ion concentration and so the Z_{eff} of the plasma is then determined. It is a common procedure to use the coronal equilibrium for the calculation of the charge distribution. The charge distribution f_{Z_i} is defined by $f_{Z_i} / \Sigma n_{zi}$, n_{zi} being the density of impurity ion with charge Z_i. Throughout this paper coronal equilibrium is taken as the equilibrium between collisional ionisation and radiative recombination, including dielectronic recombination. In reality coronal equilibrium only exists in homogeneous plasmas. In plasmas with gradients, deviations from the local coronal equilibrium occur.

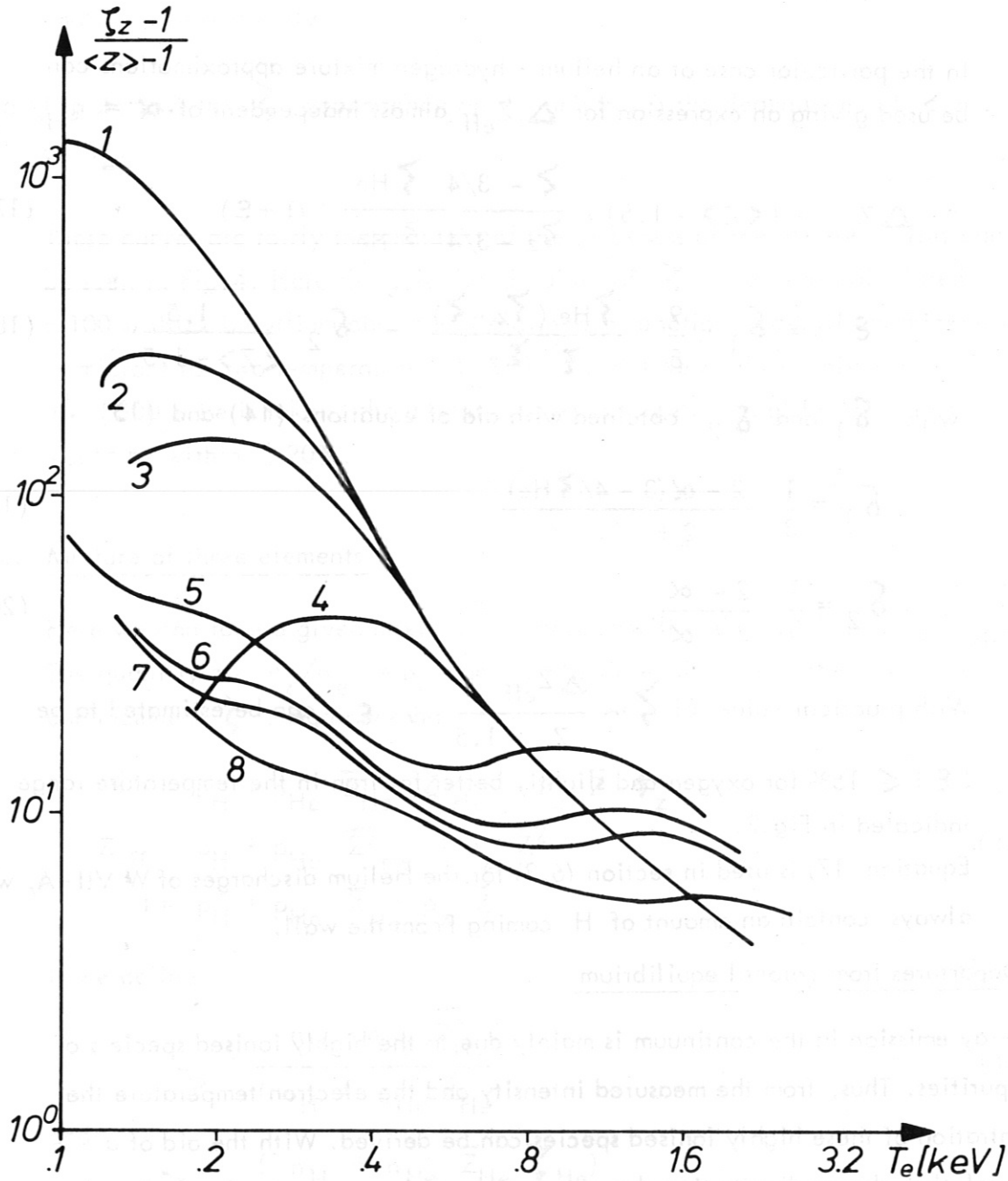

Fig.5 The relative enhancement $\frac{\zeta_z - 1}{\langle z \rangle - 1}$ as a function of the electron temperature for various departures of coronal equilibrium.
Curve 1 to 4 are for oxygen and T_e^*/T_e = 1; 0.8; 0.7; and 0.5 resp., curve 5 to 8 are for iron and T_e^*/T_e the same as above.

For steady state conditions in the central region the average ionic charge is then expected to be less, because of the inward diffusion of ions from cooler plasma regions compensating the loss due to the outward diffusion of the more highly ionised ions. In the outer regions a broadening of the charge distrubution f_{Z_i} as a function of radius can be expected, because of the inward and outward diffusion /18/.

For specific electron and ion temperatures and densities the departure from coronal equilibrium has been calculated in TFR /18/, in agreement with the experiments /24/. Also in the W VII A Stellarator /21/ and in the Pulsator Tokamak /22/ a broadening of f_{Z_i} over radius and a shift of the line emission towards the inside is observed.

In the outer plasma regions an appreciable departure from coronal equilibrium is usually found, becoming smaller towards the interior.

The higher Z-impurities have a less pronounced departure from coronal equilibrium mainly because of dielectronic recombination. Indirectly this causes higher ionisation rates thus reducing the relative importance of the diffusion.

In this paper we will not attempt a thorough analysis of the coronal equilibrium with respect to the X-ray continuum emission since such an analysis must be made for each specific case.

We shall, however, consider a small temperature change analysis for the $f_{Z_i}(T_e)$ distribution, thus simulating a departure from coronal equilibrium and enabling the influence of such a departure on the X-ray emission to be calculated.
Then, it will be shown, that for not too large departures such a change is a reasonable simulation. Here, this gives an approximate criterion for the validity of the coronal equilibrium.
We will restrict ourselves to oxygen, since it is the dominant impurity present in the W VII A device and also is the most sensitive to departures from coronal equilibrium in the temperature range of W VII A.

Fig.5 shows the influence of a small temperature change in the $f_{Z_i}(T_e)$ distribution on the calculated emission for oxygen and iron impurities; T_e being the real temperature, T_e^* being the electron temperature at which the f_{Z_i} distribution has been taken. The emission is given in units of $(\zeta_Z - 1) / (\langle Z \rangle - 1)$ as in equation (10).

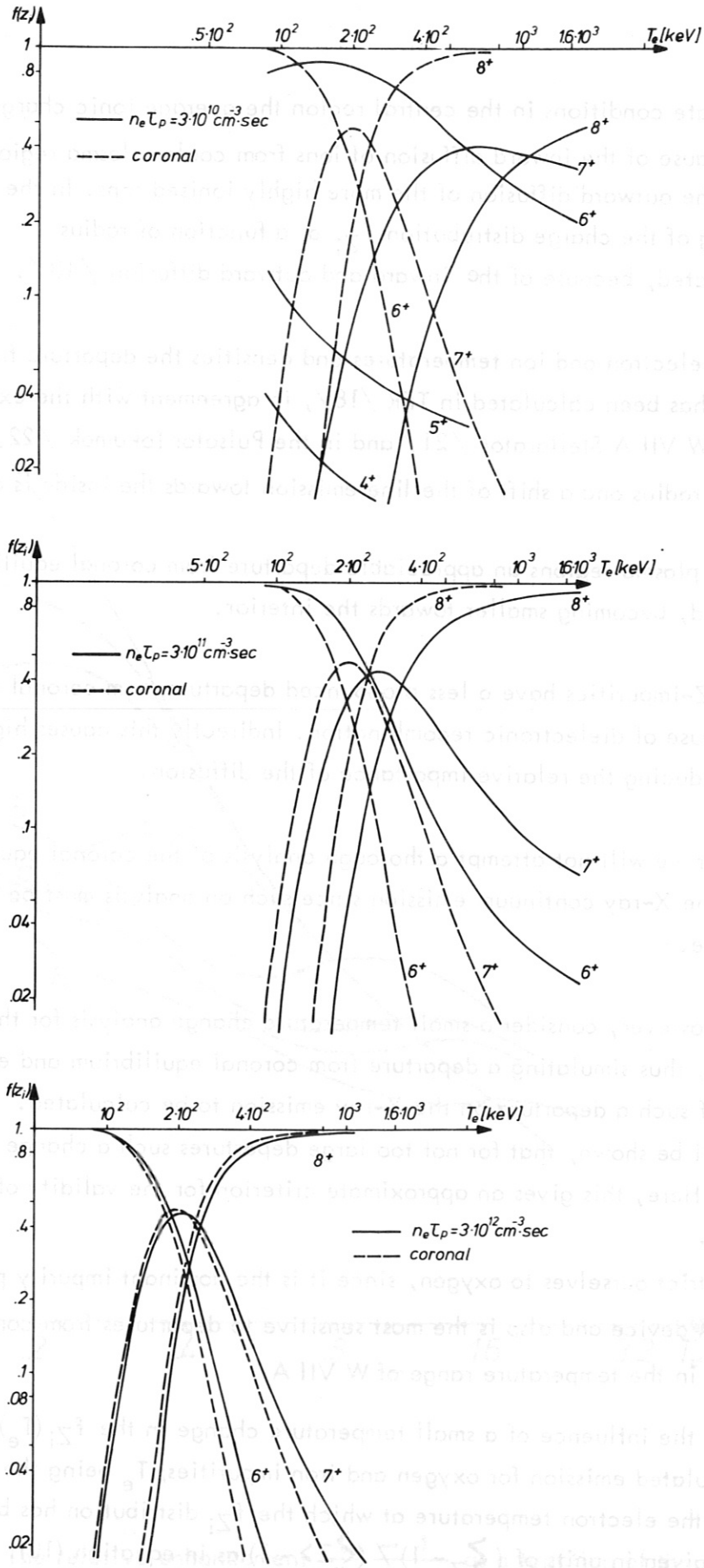

Figs.6,7,8 The departure (solid line) from coronal equilibrium (broken line) for oxygen as a function of the electron temperature T_e for various values of $n_e \tau_p = 3 \cdot 10^{12}$, $3 \cdot 10^{11}$, $3 \cdot 10^{10}$ cm^{-3} sec, resp.

For oxygen the departure from coronal equilibrium is shown in Fig.6,7 and 8 for various values of the particle lifetime. The finite lifetime is added to the particle balance equation /20/ for each species as indicated in equation (21).

For a stationary state the equilibrium situation for the ion with charge i + 1 yields the following relation:

$$n_i S_i = n_{i+1} \left(S_{i+1} + \alpha_{i+1} + \frac{1}{n_e \tau_p}\right) - n_{i+2} \alpha_{i+2} \qquad (21)$$

where S_i, α_i are the ionisation and total recombination rate cross sections, n_e is the electron density and τ_p is the particle lifetime.

An approach using finite particle lifetimes is not the best method to study the complex diffusion mechanism /18/ in the outer plasma regions. However it does give some measure of the outward diffusion at the plasma centre. Even so it will only be a rough indication of the validity of coronal equilibrium, since the inward diffusion of the lower ionised species is neglected.

Fig.9 gives the relative changed temperature T_e^*/T_e as a function of $n_e \cdot \tau_p$ (the electron density times the particle lifetime).

This figure has been obtained by shifting the coronal equilibrium distribution over a certain temperature range in such a way, that a reasonable fit is obtained with the distribution, which is calculated for a given value of $n_e \tau_p$. The lower the value of $n_e \tau_p$ is, the less accurate such a fit can be made. This increases the uncertainty in T_e^*/T_e as can be seen in Fig.9.

In the W VII A Stellarator /23/ the energy and particle confinement times increase with electron density below a certain maximum density. Below this density it follows then that departures from coronal equilibrium in the centre are not important for the X-ray emission. At lower electron densities ($n_e(o) \backsim 2 \cdot 10^{13}$ cm^{-3}) the electron temperature is relatively high ($T_e(o) \backsim 0.8$ keV), so that oxygen is fully ionised even at lower $n_e \tau_p$ values. The central value of $n_e \tau_p$ then satisfies $n_e(o) \tau_p(o) \gg n_e \tau_p(a) \backsim 10^{11}$ cm^{-3} sec. As can be seen from Fig. 5, departures from coronal equilibrium for oxygen show then little influence on the x-ray emission or ζ_z. At high densities, where confinement times are large, the value of $n_e \tau_p$ in the centre is well above $5 \cdot 10^{12}$ cm^{-3} sec, so that the departure from coronal equilibrium will be very small, even for temperatures as low as 200 eV.

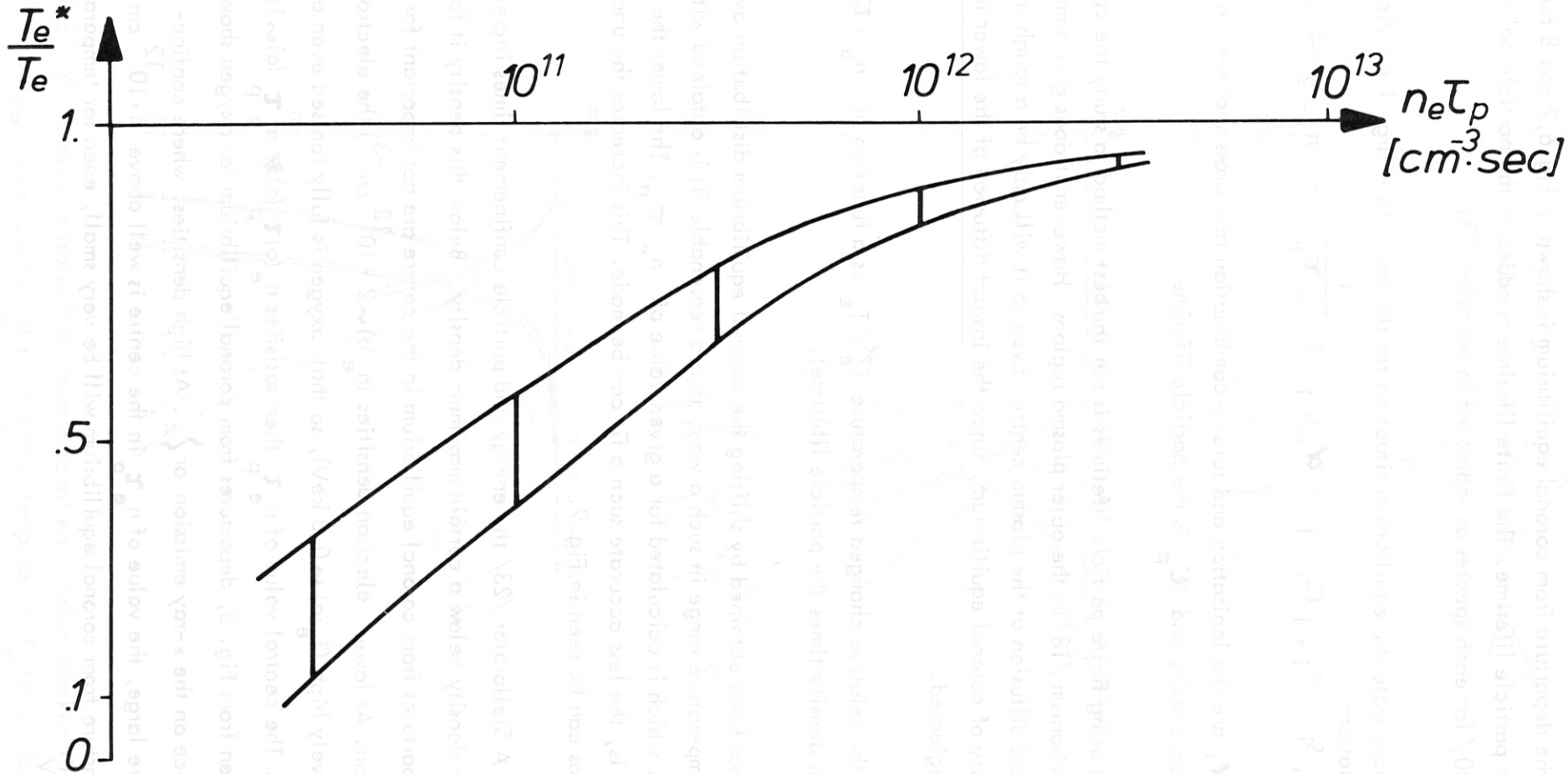

Fig.9 The estimation of the relatively changed temperature T_e^*/T_e (representing the departure from coronal equilibrium) as a function of $n_e \tau_p$ for the oxygen impurity.

In the outer regions the coronal equilbrium does not hold since here the electron density and particle confinement time decrease with increasing radius.

The complex nature of the diffusion mechanisms makes the simple approach as used above impossible at low values of $n_e \tau_p$. Two possible solutions of this problem have been indicated in /18/: i.e. the exact determination of the f_{Z_i} distribution by calculation or its determination by spectroscopic measurements either in the VUV or in the X-ray domain /12, 13/, In both cases the electron temperature and electron density radial profiles must be known.
However, in the following chapters we will restrict ourselves to the coronal equilibrium charge distribution, and thus, in the case of W VII A, to the central part of the ohmically heated discharge.

4. Approximations for the intensity of continuum emission

Approximations will be used in the following chapters to study the influence of line radiation and of the radial profiles on the filter method, because the use of equation (3) would be rather cumbersome.
These approximations can also be used to choose the optimum filter type and thickness for any specific experiment.

Two types of approximation will be given: an accurate one, which can be handled by a small computer and a simple one, which permits a study of the interdependence of several parameters.

4.1. Accurate approximation

This approximation is obtained from the calculated intensities, according to formula (3).

A best fit is made over the electron temperature range of interest. In the case of the W VII A Stellarator we have made the fit over $0.1\ \text{keV} < T_e < 1\ \text{keV}$.

The continuum emission from a hydrogen plasma through a beryllium filter can then be written as

$$I = 2.4 \cdot 10^{-16}\ n_e^2\ f(T_e)\ \sqrt{T_e}\ \exp\left(-\left(\frac{T_c}{T_e}\right)^{\alpha}\right)\ \frac{\text{keV}}{\text{cm}^3\,\text{ster sec}} \qquad (22)$$

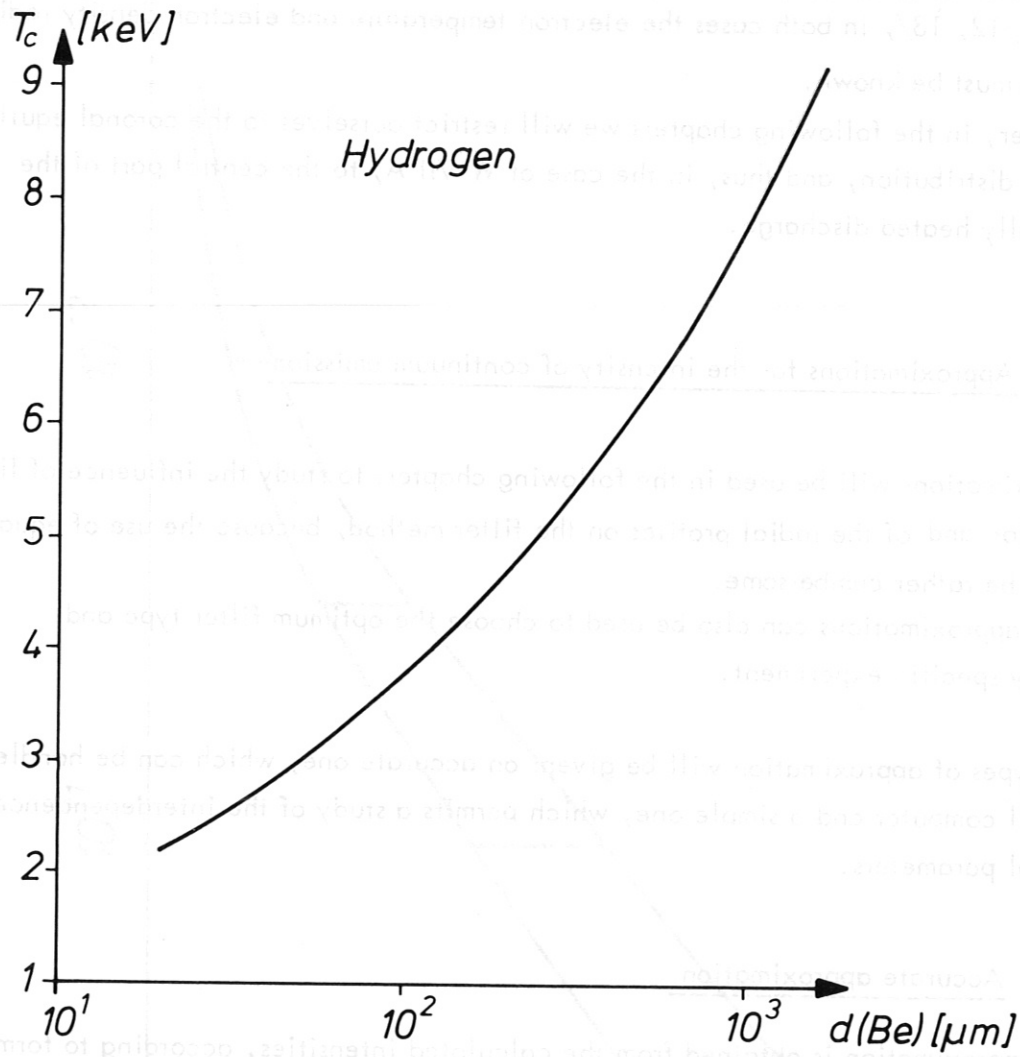

Fig. 10 The characteristic cut-off energy T_c in keV as a function of the beryllium thickness in μm for the accurate approximation of the hydrogen emission.

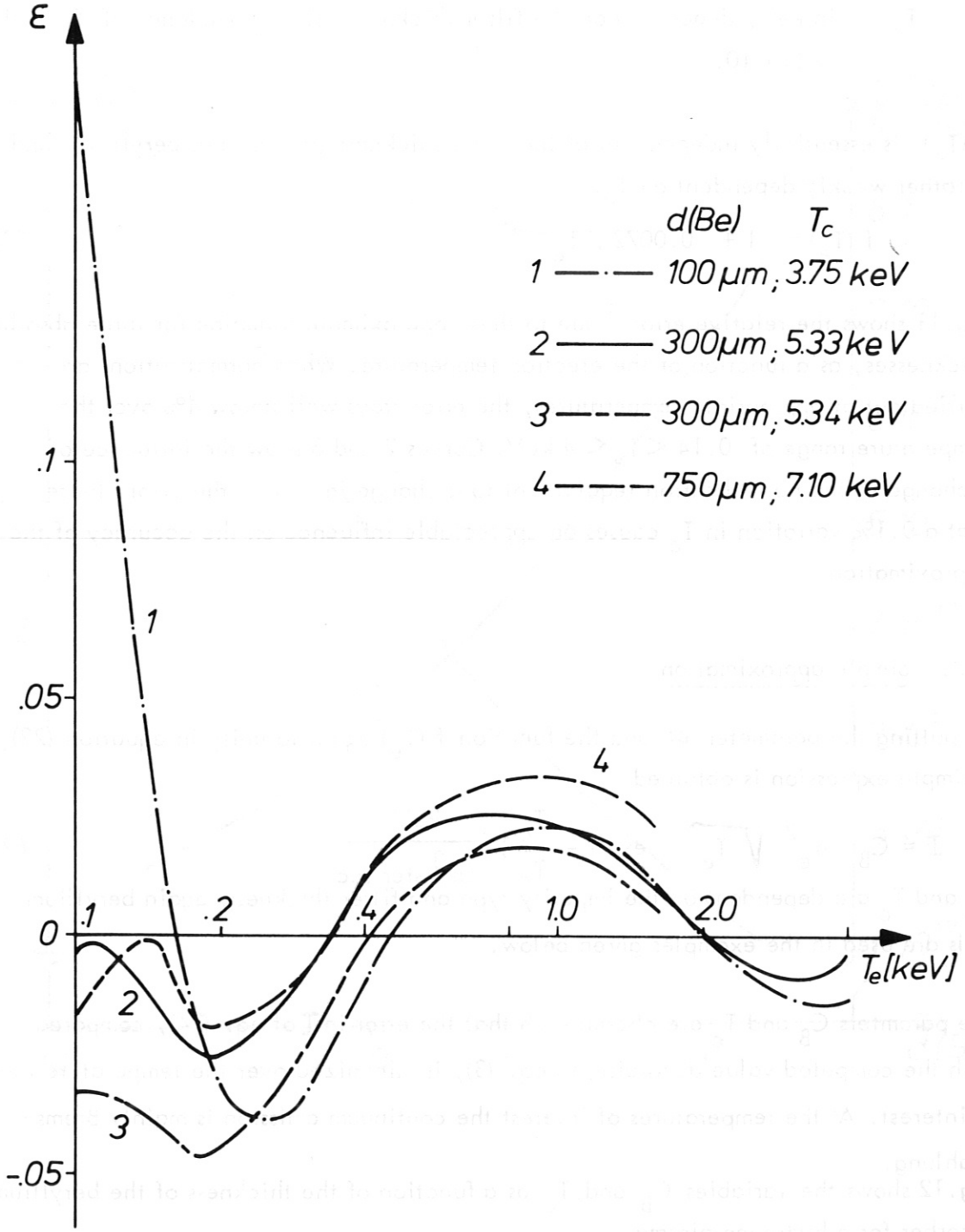

Fig.11 The relative error ε of the approximation in Fig.10 as a function of the electron temperature T_e for various thicknesses of the beryllium filter.

T_e : electron temperature in keV

n_e : electron density in cm^{-3}

α : 0.79

T_c : in keV, depending on the filter thickness. This dependence of T_c is shown in Fig.10.

$f(T_e)$ is essentially independent of the filter thickness (in our case beryllium) and is rather weakly dependent on T_e:

$$f(T_e) = 1 + 0.0072 / T_e^{2.46} \qquad (23)$$

Fig.11 shows the relative error[+)] due to these approximate formulae for three absorber thicknesses, as a function of the electron temperature. When normalisations are carried out at appropriate temperatures, the error stays well below 4% over the temperature range of $0.14 < T_e < 4$ keV. Curves 2 and 3 show the influence of a change in the normalisation (equivalent to a change in T_c) on the error. Note that a 0.1% variation in T_c causes an appreciable influence on the accuracy of the approximation.

4.2. Simple approximation

By putting the parameter α and the function $f(T_e)$ equal to unity in equation (22), a simple expression is obtained

$$I = C_B \; n_e^2 \sqrt{T_e} \; \exp\left(-\frac{T_c}{T_e}\right) \; \frac{\text{keV}}{\text{cm}^3 \text{ ster sec}} \qquad (24)$$

C_B and T_c are dependent on the impurity type and filter thickness; again beryllium foils are used in the examples given below.

The paramters C_B and T_c are chosen such that the error in I of eq. (24), compared with the computed value according to eq. (3), is minimized over the temperature range of interest. At the temperatures of interest the continuum emission is mainly Bremsstrahlung.
Fig.12 shows the variables C_B and T_c as a function of the thickness of the beryllium absorber for a hydrogen plasma.

+) The relative error is defined as the approximate intensity minus the computed intensity over the computed intensity.

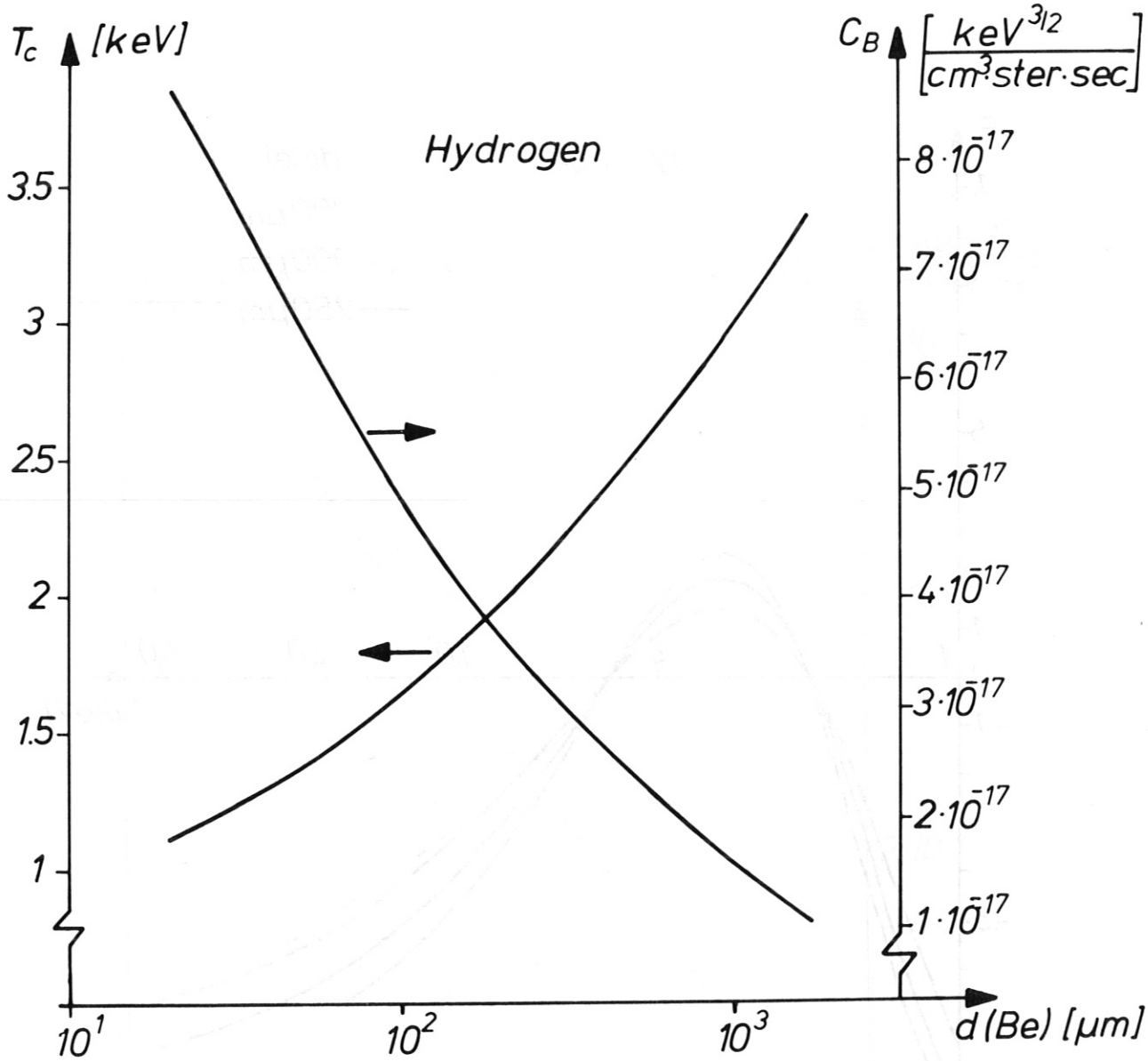

Fig. 12 The characteristic cut-off energy T_c in keV and the variable C_B as a function of the beryllium thickness in μm for the simple approximation of the hydrogenic emission.

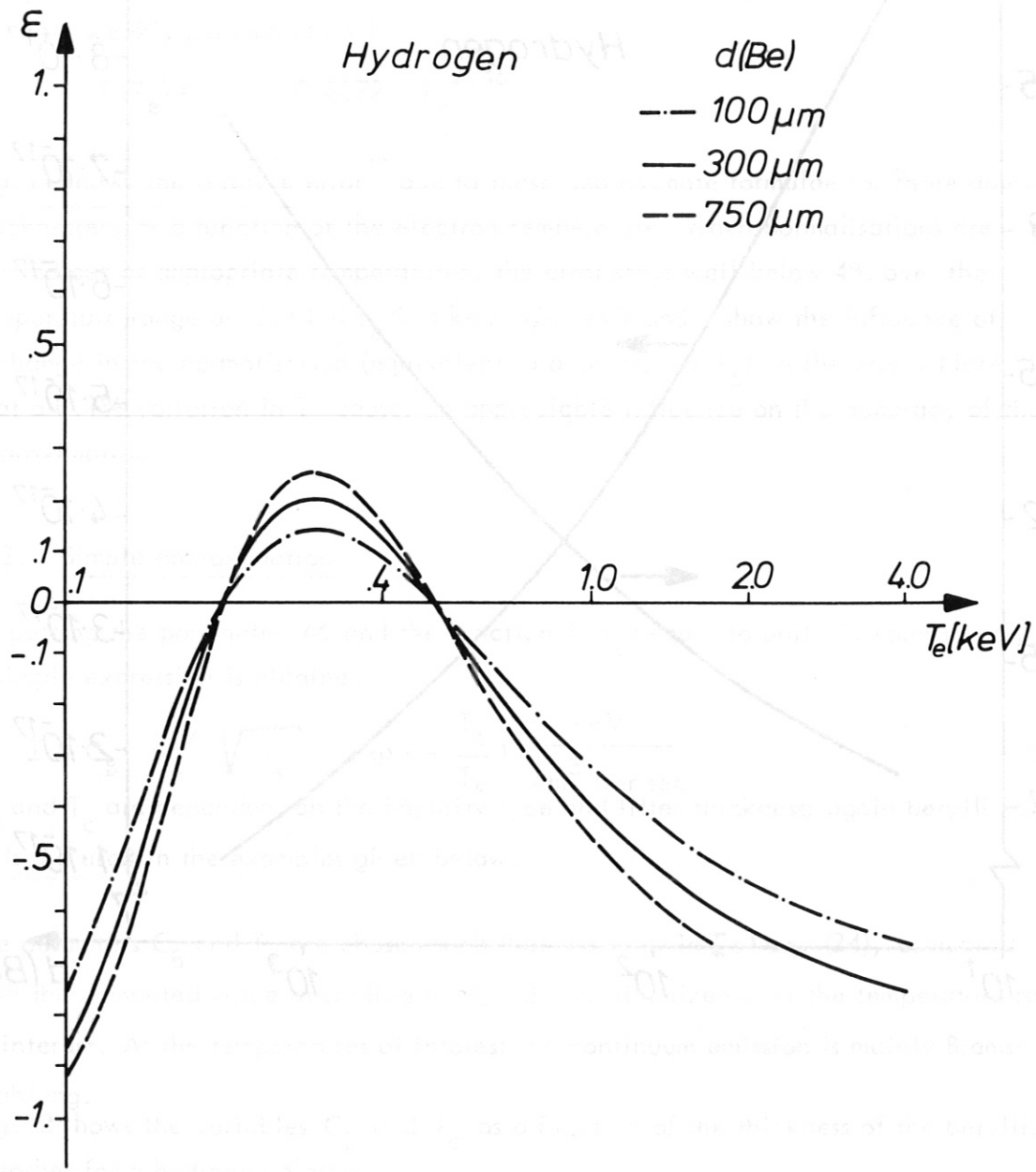

Fig. 13 The relative error ε of the approximation in Fig. 12 as a function of the electron temperature T_e for various thicknesses of the beryllium filter.

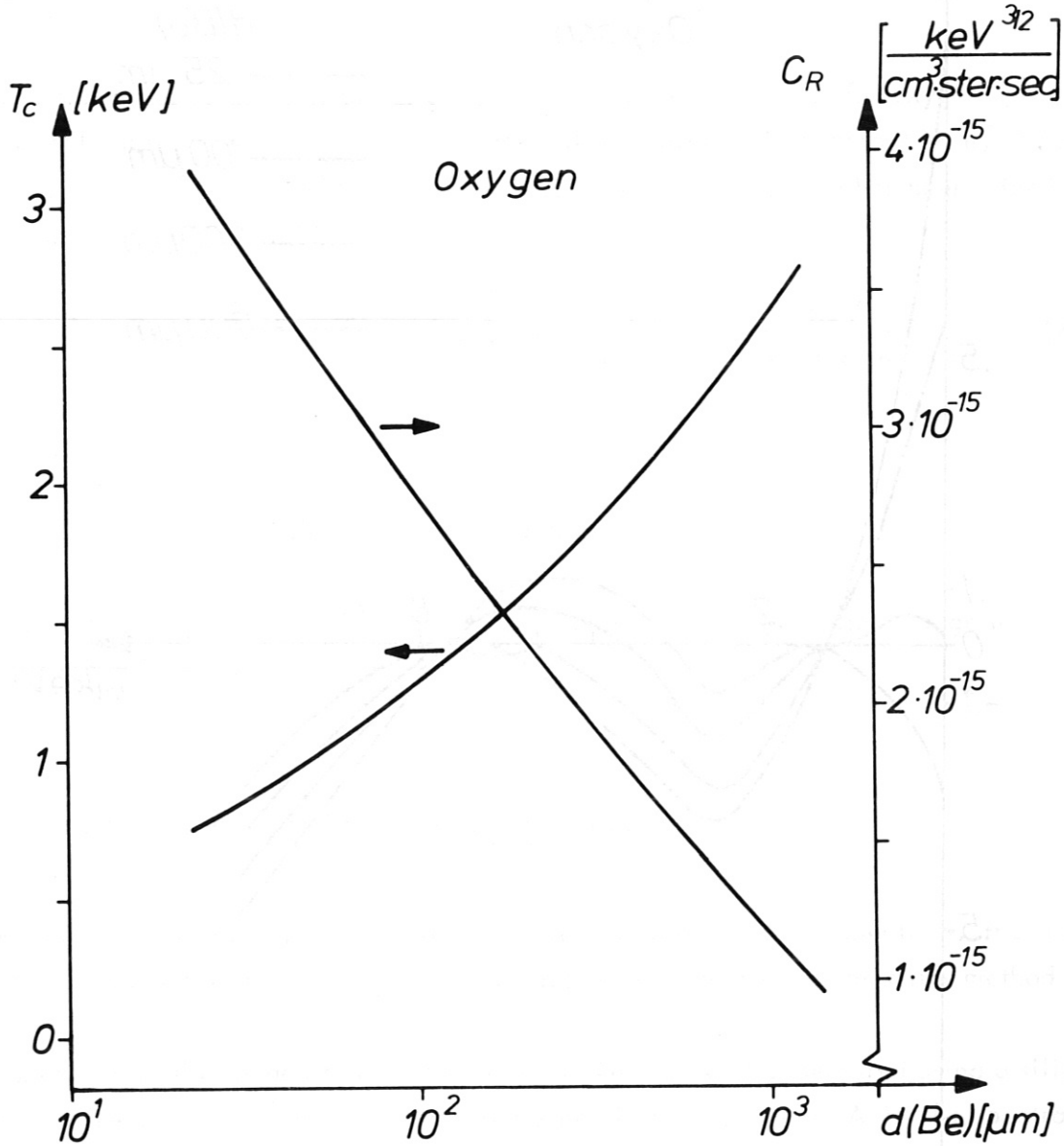

Fig.14 The characteristic cut-off energy T_c and the variable C_R as a function of the beryllium thickness for the approximation for the X-ray emission for oxygen in coronal equilibrium.

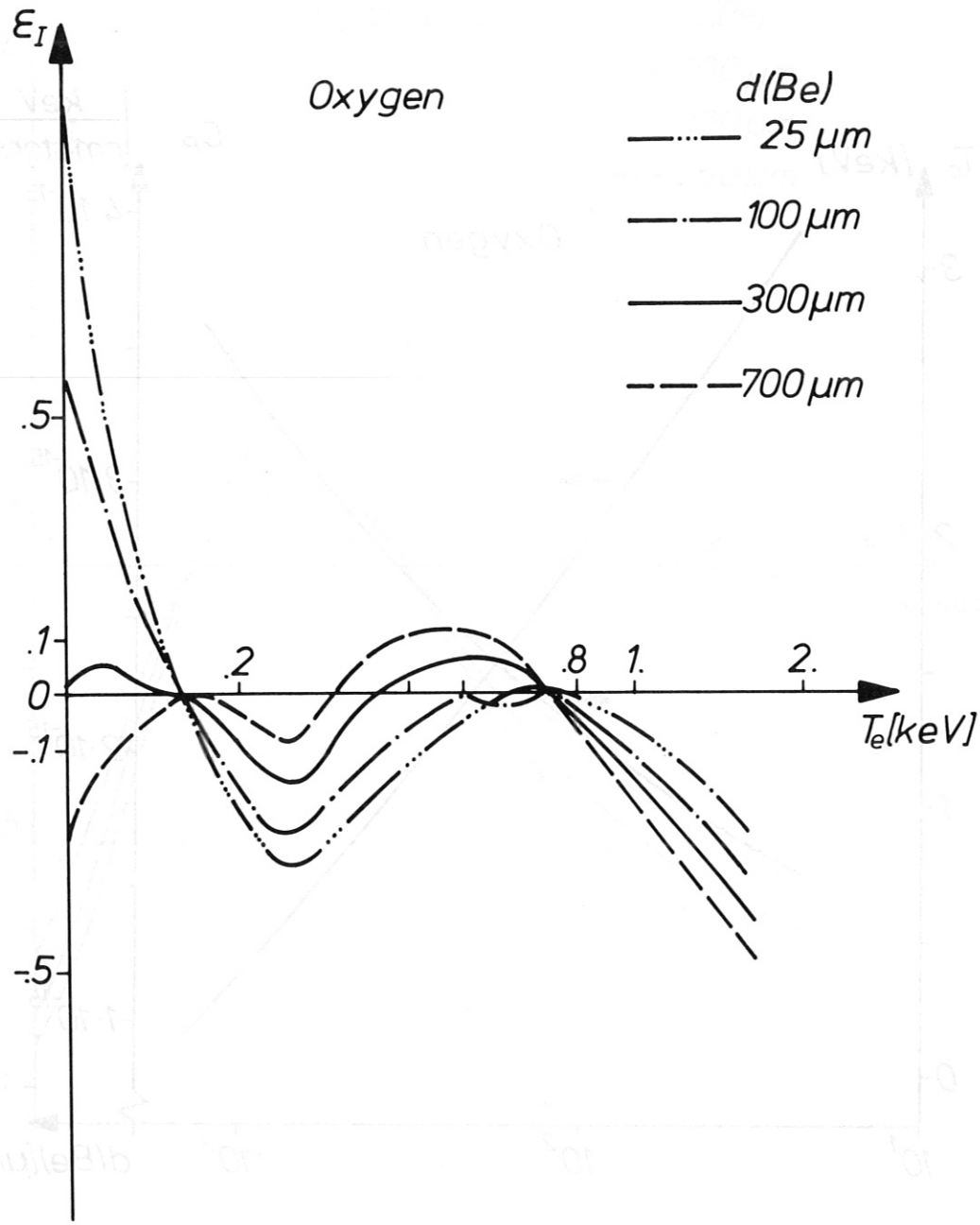

Fig.15 The relative error ε_I of the approximation in Fig.14 as a function of the electron temperature T_e for various thicknesses of the beryllium filter.

The relative error ε as a function of the electron temperature is given in Fig.13 for three foil thicknesses: 100, 300 and 750 μ.

If we accept an error of $\pm$ 25%, we find the temperature range over which this approximation is valid to be 170 eV $< T_e <$ 700 eV. Thus an analytic study can be made, particularly with respect to the line radiation treated in chapter 5.2.

Since oxygen is the dominant impurity, Fig.14 gives the variables C_R and T for oxygen as a function of the thickness of the beryllium foil.

Fig.15 shows the relative error ε_I again versus temperature and for oxygen in coronal equilibrium. Because the recombination radiation is dominant here,[x] at least for temperatures below 1.5 keV, the square root of the temperature has been added to the denominator. This yields:

$$I = C_R \; n_e^2 \; P_{ox} \; \bar{Z} \exp\left(-\frac{T_c}{T_e}\right) \cdot \frac{1}{\sqrt{T_e}} \quad \frac{\text{keV}}{\text{cm}^3 \text{ sec ster}} \qquad (25)$$

where $P_{ox} = n_{ox} / n_e$

$\bar{Z}$ = average charge of the oxygen ion

Thus a reasonable approximation can be found over a large temperature range for various foil thicknesses (Fig.15).

5. The filter method and the electron temperature

One method of measuring electron temperature is to use the X-ray spectrum. The spectrum can be obtained both by direct and by indirect measurement (i.e. the filter method /3/).

The spectrum in the range of 0.7 keV to $\sim$ 30 keV is usually measured using a silicion lithium drifted detector (Si (Li)) and a pulse height analyser (P.H.A.). The spectral resolution is limited to 150 eV at 5.9 keV. If better resolution is required, a curved crystal spectrograph is employed. The different ionisation stages of the iron and molybdenum impurity have been measured with such an instrument in the ST, PLT and TFR tokamaks /13, 25, 26/.

x) The transition temperature above which the Bremsstrahlung starts to dominate the continuum emission is roughly given by : $T_e \sim 2 Z^2 I_H$

However the better spectral resolution is obtained at the cost of the large X-ray energy range. The curved crystal spectrometer can only cover a range of typically $\sim$ 0.5 keV with one crystal.

Both the Si (Li) detector and the curved crystal spectrometer are usually operated in the P.H.A. mode and are therefore low flux instruments.

This implies that the time resolution will not be better than a few milliseconds (typically $\sim$ 5 msec). Also many reproducible discharges are needed in order to get sufficient counts per energy channel. Further to avoid pulse pile-up problems count rates have to be typically less than 30 kilocounts per second. It is thus evident that these instruments cannot be used as a plasma monitor device on a shot to shot basis. However an alternative technique is the determination of the electron temperature by the filter method.

If two filters are used, the necessary assumption of a Maxwellian plasma must be verified, for example by measurements with a Si (Li) spectrometer. Also in order to make the filter method relatively independent of the impurity type, filter thicknesses have to be chosen such that free-bound discontinuities lie outside the energy range seen by the detectors.

The limitations and influence of line radiation and the integration over the volume (or line) of sight will be treated in the following chapters 5.2. and 5.3. With the aid of the known electron density and with two filters, the following two plasma parameters can be obtained: the enhancement factor ζ of the intensity and the electron temperature.

5.1. The influence of the impurity type on the filter method

The influence of the impurity type and the effect of departure from coronal equilibrium on the ratio R of the fluxes passing through two separate filters as a function of the electron temperature is studied. An analytic approximation to the function $R(T_e)$ is made.

It follows from equation (22), that

$$R(T_e) \simeq \exp\left(\left(\frac{A}{T_e}\right)^{\alpha}\right) \qquad (26)$$

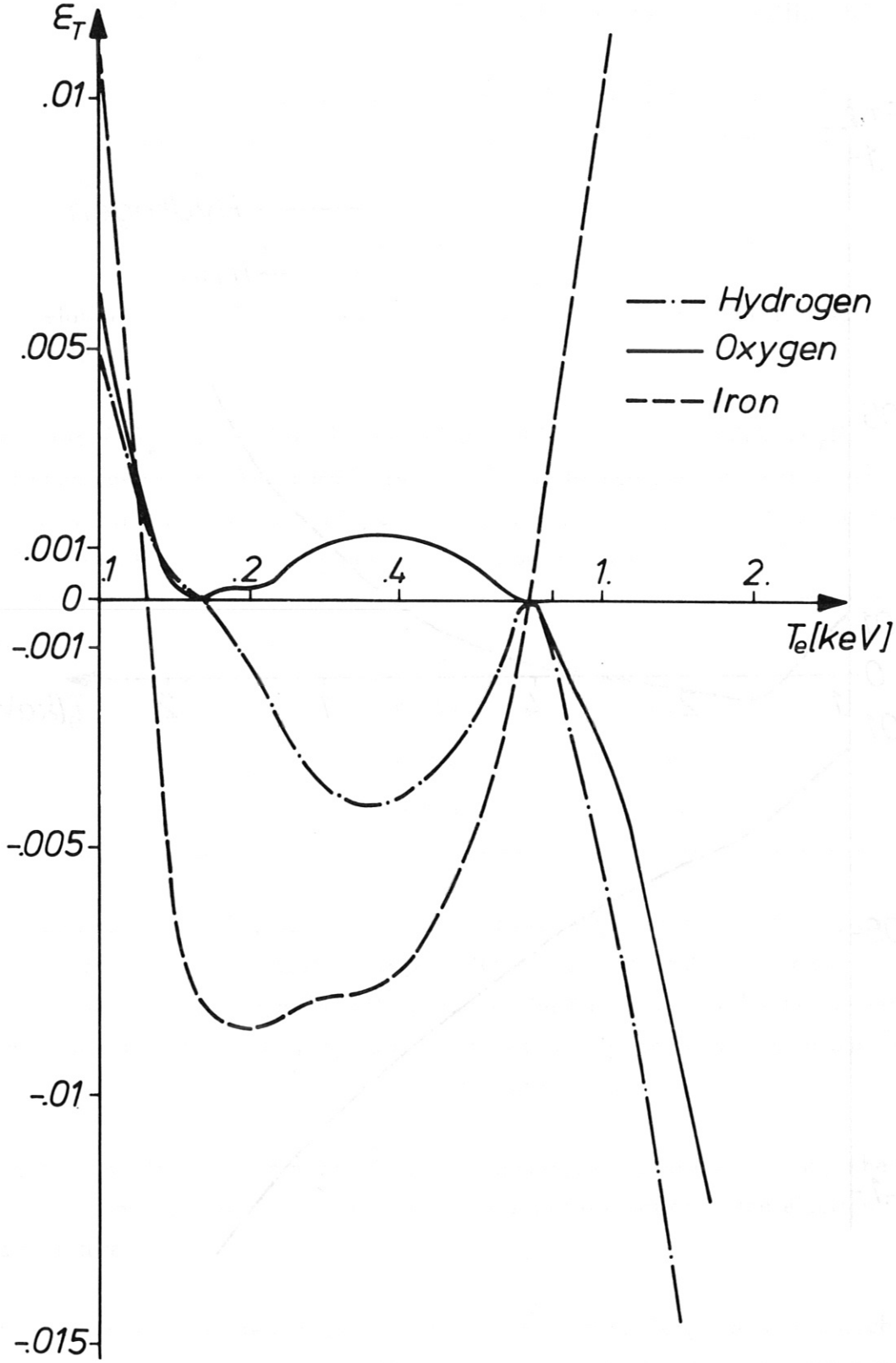

Fig. 16 The relative error ε_T in the electron temperature T_e as a function of T_e, when using the approximation instead of the computer values of $R(T_e)$ for various elements.

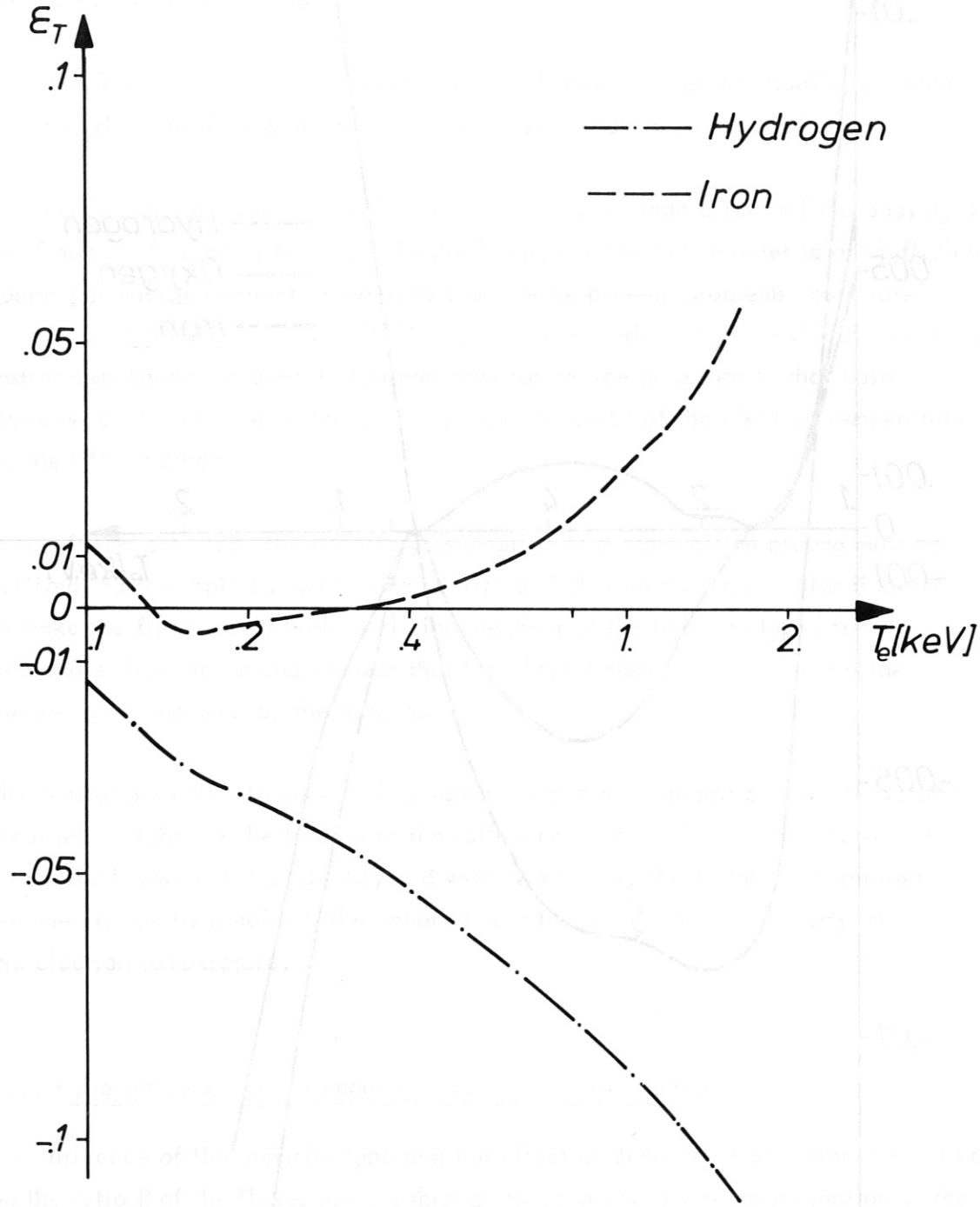

Fig. 17 The relative error ε_T in T_e as a function of T_e, when using the approximation for oxygen of $R(T_e)$ also for hydrogen and iron.

with α as in (22) and A given by the T_c's belonging to each beryllium filter.

The parameters α and A are determined from the calculated $R(T_e)$'s for hydrogen, oxygen and iron in coronal equilibrium. Then for a given R T_e is calculated accordingly:

$$T_e = A / (\ln R)^{1/\alpha} \qquad (27)$$

The relative error[+] ε_T between this calculated T_e and the real T_e is given in Fig.16.

The ratio $R(T_e)$ for the flux through a 326 μ thick to a 738 μ thick beryllium filter has been calculated. This combination is suitable to measure the electron temperature in the W VII A device, with temperatures between 0.2 and 0.8 keV. The parameters α and A for each impurity are given in table I below.

TABLE I

	α	A (keV)
hydrogen	0.79199	0.83769
oxygen	0.81612	0.77289
iron	0.82138	0.76225

As can be seen from Fig.16 an extremely accurate approximation is found, especially for oxygen over the temperature range of 100 eV to 1.26 keV (better than $5 \cdot 10^{-3}$). We will therefore use equation (26) to obtain the differences in the determined T_e, when using the various $R(T_e)$, calculated numerically for the various impurities and for various departures from the coronal equilibrium.

Fig.17 shows the relative error ε_T for a hydrogen and an iron plasma, when using the approximate $R(T_e)$ for oxygen, again as a function of the electron temperature.

It follows that when the enhancement factor ζ is much larger than one (such that hydrogen emission is negligible), the $R(T_e)$ of oxygen yields an accurate electron temperature (better than 2%). The condition for the enhancement of the radiation over that of a hydrogen plasma ($\zeta \gg 1$) is readily fulfilled for plasmas with

---

[+] This relative error is defined as the apparent temperature minus the real temperature over the real temperature.

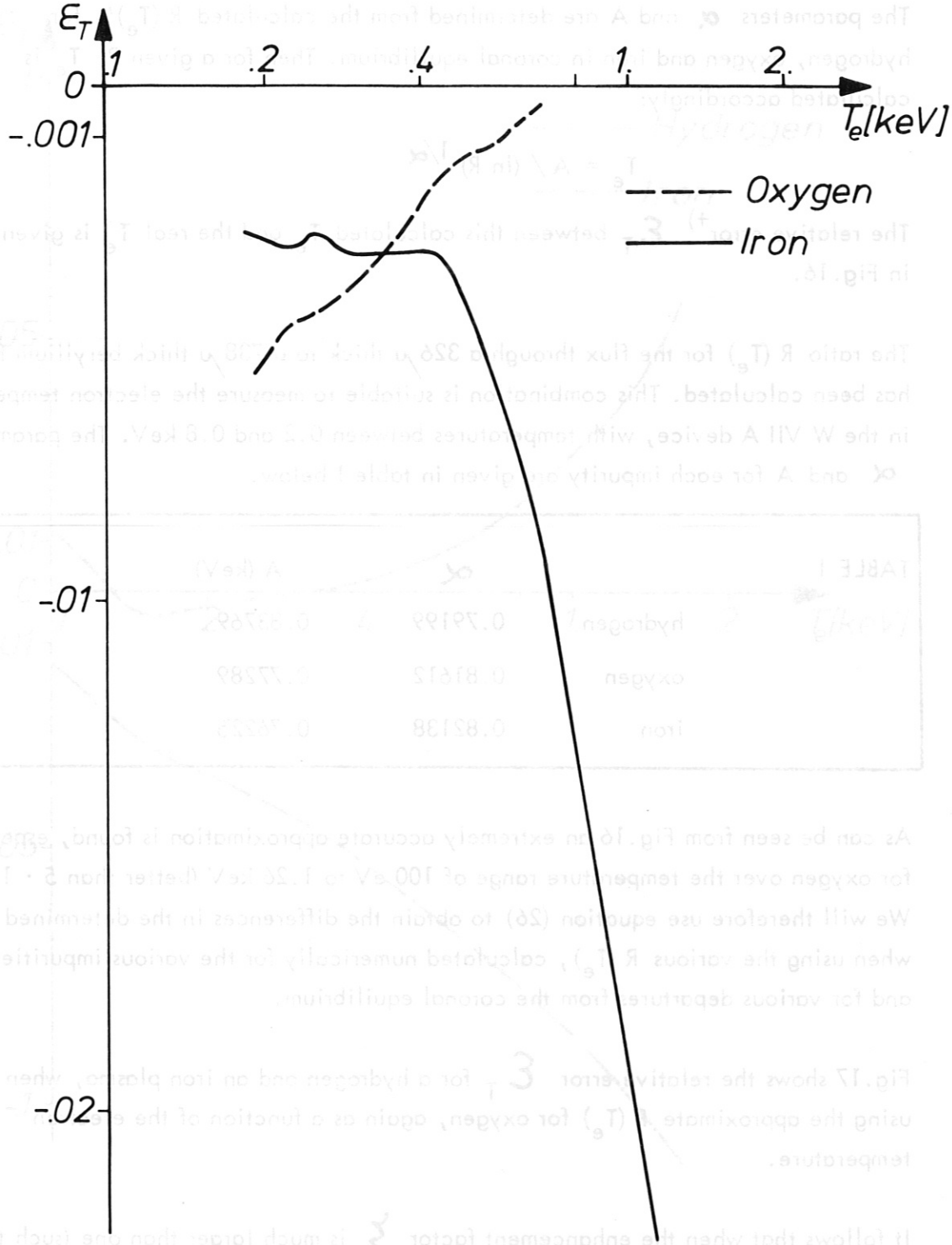

Fig. 18 The influence of departures in coronal equilibrium on the filter method for oxygen and iron. The departure is simulated by taking $T_e^*/T_e = 0.5$ and by calculating the relative error ε_T in T_e as a function of T_e when using the coronal equilibrium dependence of $R(T_e)$ instead of $R(T_e)$ calculated for the departure of coronal equilibrium

T_e below 1 keV (usually $\gtrsim$ 10, even for Z_{eff} close to one).

Departures from coronal equilibrium are only causing small changes in the filter combination function R (T_e). This is shown in Fig. 18. The relative error in the electron temperature is given as a function of T_e for oxygen and iron resp. It is calculated from eq. (27), using the R (T_e), that is computed for an ionic charge distribution, which departs from coronal equilibrium according to section (3.3) with $T_e^*/T_e = 0.5$. The errors are well below one percent in the temperature range of interest.

5.2. The influence of the impurity line radiation on the filter method

Thermal X-ray spectra usually show a continuum with superimposed impurity lines /1, 7, 8/. The impurity lines are due to oxygen, stainless steel and molybdenum, the wall materials, present in the plasma.

The strongest are Cr and Fe - L-lines around 1 keV, Mo-L-lines around 2.4 keV and the Cr and Fe-K α-lines. The electron temperatures in present devices are two small to excite the Mo-K-lines, except in the case of a non-thermal electron distribution /7/. Non-thermal plasmas usually occur for electron densities below about $n_e = 10^{13} cm^{-3}$. For the higher densities of interest for fusion research thermal X-ray spectra are usually obtained.

The X-ray spectra of W VII A show features similar to those of ST, TFR and Pulsator (see Figs. 32 and 33). Because of lower electron temperatures no excitation of the chromium and iron K-lines occurs. In general, for energies above the last impurity line (in our case the Mo-L-line), the X-ray spectrum is a thermal continuum. This spectral range we will use to obtain the electron temperature by the filter method. Therefore we must use filters which eliminate the 2.4 keV Mo-L-line.

Because of the drastic decrease in the flux (see equation (25)) with increasing foil thickness and decreasing electron temperature, there is a limitation on the foil thickness which can be used.

Also it would not be suitable to have the cut-off energies of the two filters too close to each other. This would mean that the factor A in equation (26) is small and hence a low precision in the temperature determination would result.

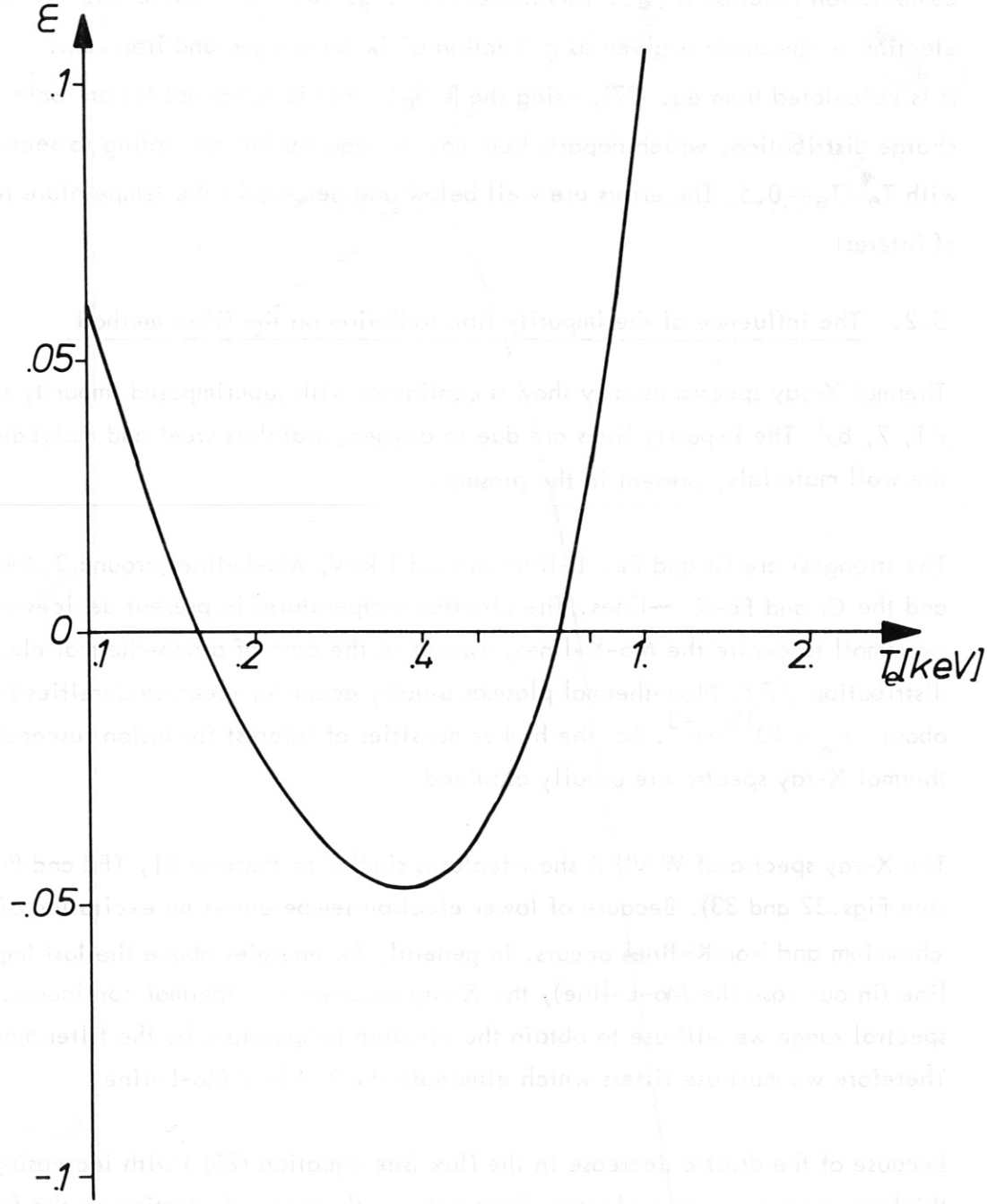

Fig. 19 The relative error in T_e as a function of T_e for the simplified approximation of $R(T_e)$ for oxygen.

Thus it is likely that the thinner of the two filters passes some of the impurity line radiation. As an example the effect of the Mo-L-line on the filter method (326 and 738 μ thick beryllium foils) will be studied.

Assuming that oxygen is the dominant impurity, equation (25) is taken for the continuum emission.

The cross-sections for the molybdenum L-line emission are not well-known. Estimates based on the formulas given in /12/ and /20/ show that, as for the Fe-K_α -line, dielectronic recombination is probably the most important contributor. (For $T_e \backsim 0,5$ keV it is around a factor of 4 more than collisional excitation). Since we are mainly interested in the temperature dependence of the line emission, we have taken

$$S\,(Mo\text{-}L) = n_e\, n_{Mo} \cdot C_{Mo}\, \frac{e^{\frac{-2.4}{T_e}}}{T_e^{3/2}} \quad \frac{keV}{cm^3\ ster\ sec} \tag{28}$$

with $$C_{Mo} = 2.10^{-11}\ \frac{keV^{5/2} cm^3}{sec\ ster}$$

C_{Mo} was obtained from equations (4) and (6) from Breton et al /20/ by putting f_{z_i}, the oscillator strength, equal to one and taking

$$(Z+1)^2 = \frac{\Delta E}{(\frac{1}{n^2} - \frac{1}{(n+1)^2})\, I_H}$$

where ΔE = the energy of the molybdenum L-line. In our case $\Delta E \backsim 2.4$ keV, as measured by the Si (Li) spectrometer in the W VII A device.

It is believed that equation (28) yields the correct order of magnitude of the molybdenum concentration.

By using the continuum emission equation (25) instead of eq. (3), one gets to a good approximation $R\,(T_e)$ as follows :

$$R\,(T_e) = 1.4\, e^{\frac{0.524}{T_e}} \tag{29}$$

for the 326 and 738 μ beryllium filters. The relative error in T_e compared to the numerically calculated value is given in Fig.19 and, for the temperature range of interest, is less than 5%.

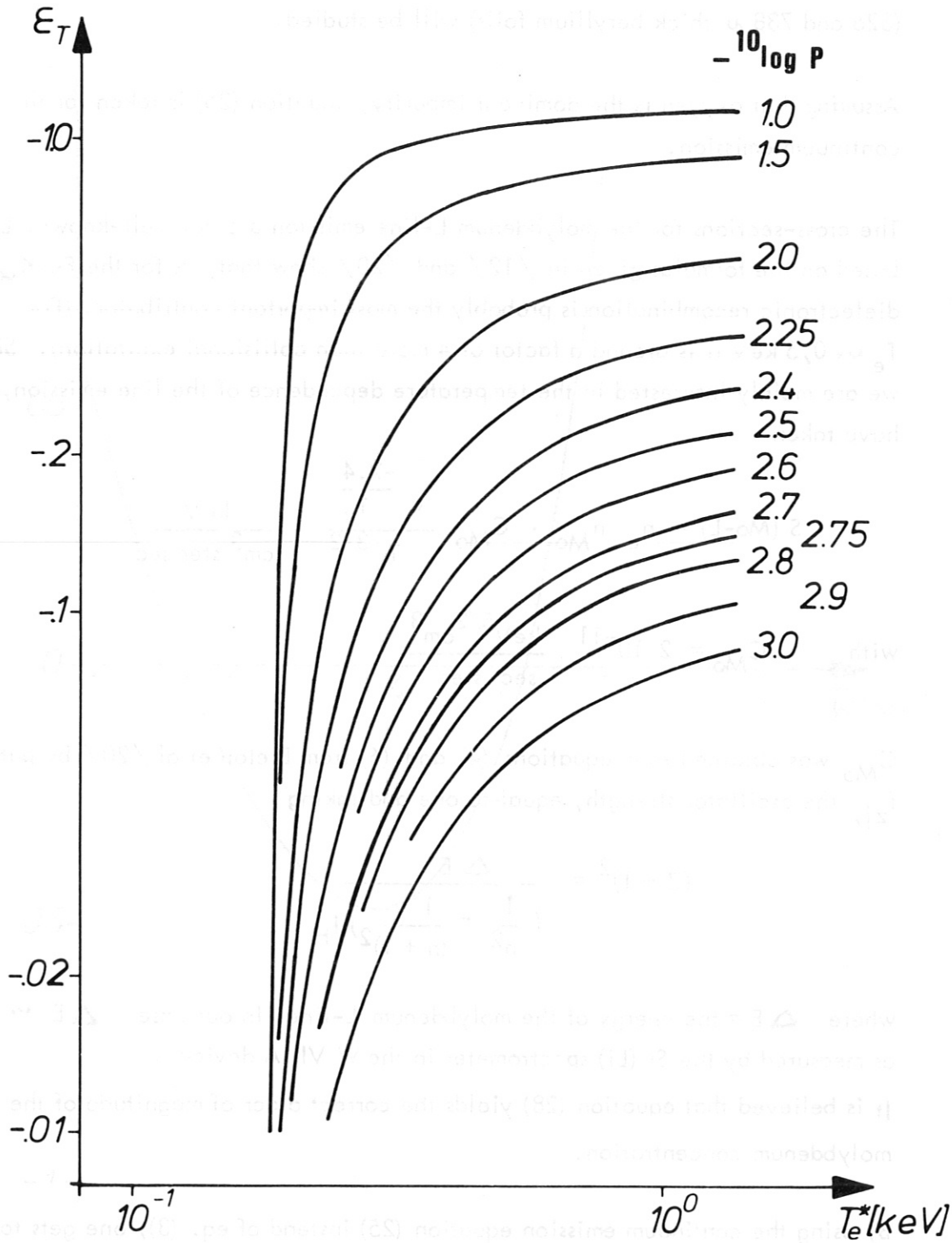

Fig.20 The relative error in T_e: $\mathcal{E}_T(p,T_e^*)$ due to line radiation as a function of the apparent temperature T_e^* for various concentrations p of molybdenum.

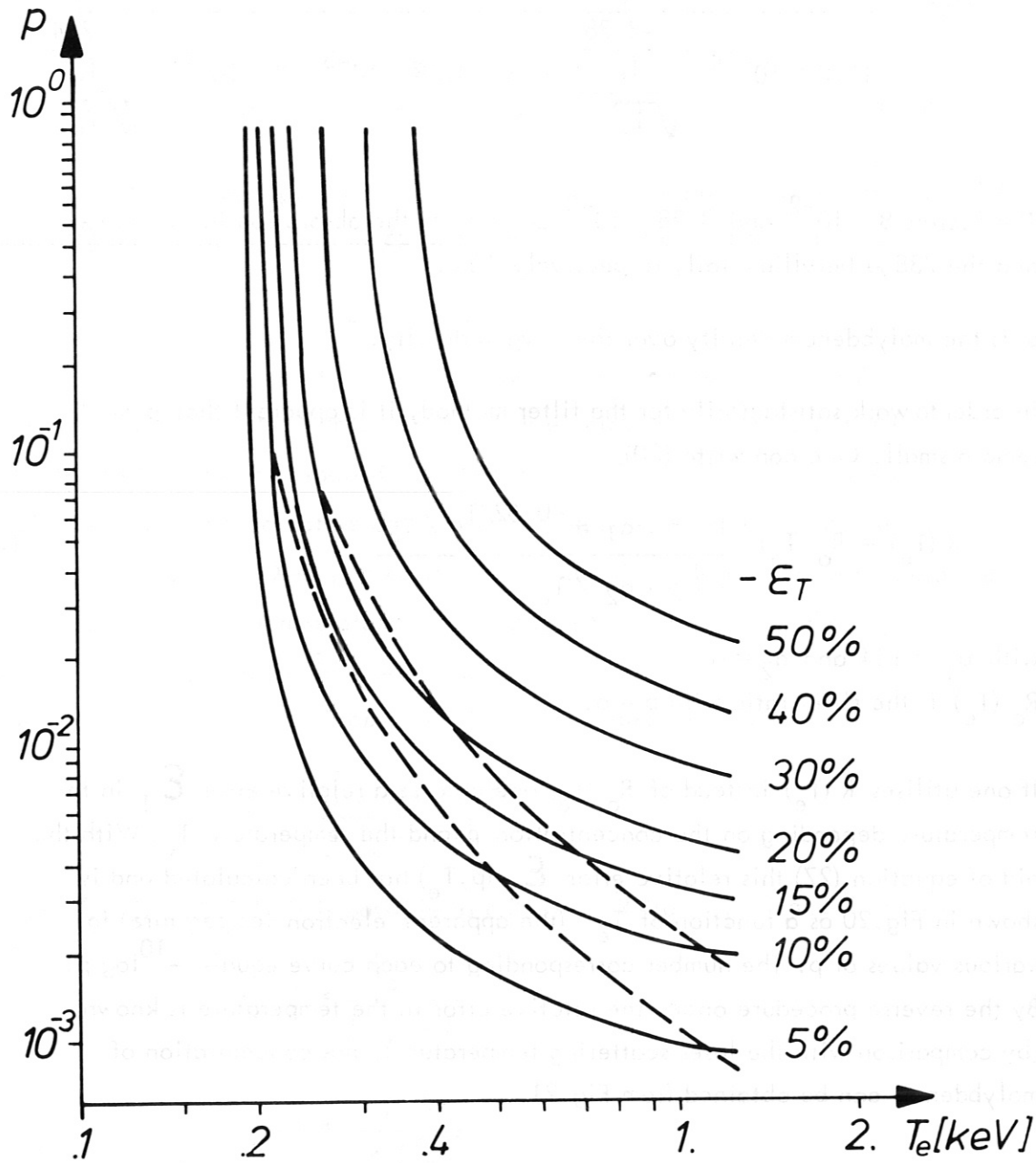

Fig.21 The relative error in T_e: $\varepsilon_T(p,T_e)$ due to line radiation as a function of the molybdenum concentration p and the real electron temperature T_e (full lines).

Therefore we obtain the ratio $R(T_e)$, this time including the line radiation, in a simple way by multiplying C_R of eq. (25) with $\overline{Z}$. This yields :

$$R(T_e) = \frac{1.54 \quad 10^{-14} \; e^{\frac{-1.86}{T_e}} / \sqrt{T_e} \; + \; p \cdot 8 \; 10^{-2} \cdot 2 \quad 10^{-11} \; e^{\frac{-2.4}{T_e}} / \sqrt[3]{T_e}}{1.10 \quad 10^{-14} \; e^{\frac{-2.38}{T_e}} / \sqrt{T_e} \; + \; p \cdot 3.28 \quad 10^{-3} \cdot 2 \quad 10^{-11} \; e^{\frac{-2.4}{T_e}} / \sqrt[3]{T_e}} \qquad (30)$$

The factors $8 \quad 10^{-2}$ and $3.28 \quad 10^{-3}$ come from the absorption in the 320 μ and the 738 μ beryllium foil, respectively /5/.

p is the molybdenum density over the oxygen density.

In order to work satisfactorily for the filter method, it is apparent that p must remain small. One can write (30):

$$R(T_e) = R_o(T_e) \; \frac{1 + p \cdot a_1 \; e^{-0.52/T_e} / T_e}{1 + p \cdot a_2 / T_e} \qquad (31)$$

with $a_1 = 104$ and $a_2 = 6$.
$R_o(T_e)$ is the filter ratio with $p = o$.

If one utilises $R(T_e)$ instead of $R_o(T_e)$ one creates a relative error ε_T in the temperature depending on the concentration p and the temperature T_e. With the aid of equation (27) this relative error $\varepsilon_T(p, T_e)$ has been calculated and is shown in Fig.20 as a function of T_e (the apparent electron temperature) for various values of p. The number corresponding to each curve equals $-^{10}\log p$. By the reverse procedure once the relative error in the temperature is known (by comparison with the laser scattering temperature), the concentration of molybdenum can be obtained from Fig.21.

Here the relative concentration p of molybdenum is given as a function of the electron temperature for various relative errors in the temperature ($-\varepsilon_T$ = 5, 10, 20, 30, 40, 50%; solid lines). The broken lines are obtained if the collisional excitation (equation (9) of ref./20/ with $f\bar{g} \backsim 0.35$ /8/) is used instead of the dielectronic recombination as the source of the line emission. The lower broken curve is for ε_T = - 5% and the upper for ε_T = -10%.

This shows that even if the wrong emission mechanism is used, the same order of magnitude for the molybdenum concentration is obtained.

5.3. The influence of the radial profiles on the filter method

The best way to obtain a spatially resolved X-ray emission intensity from line or volume integrated flux measurement is by Abel inversion of the measured flux profiles.

A good Abel inversion is only possible, if the spatial resolution is satisfactory /27/. Typically the spatial resolution Δ at the plasma centre must be kept small.

$$\Delta \leq 2\,a / N \tag{32}$$

where a is the plasma radius and N is the number of grid points of the Abel inversion. In case of thick absorbers and low electron temperatures, it is not possible to maintain good spatial resolution and a measurable flux. A normal Abel inversion can then not be carried out. Therefore we have studied here the influence of the radial X-ray intensity profile and the radial electron temperature profile on the central temperature determination from the filter method by taking bell shaped analytical fits for these profiles.

The ratio of the flux through absorber 1 and 2 is then given by:

$$\bar{R} = \frac{\int I_1(r)\; d^3 r}{\int I_2(r)\; d^3 r} \tag{33}$$

Since $I_2 = I_1 / R\,(T_e)$, it is possible to calculate $\bar{R}$ from I_1 (r) and T_e(r); by taking

$$I_1\,(r) = \frac{I_o}{1 + (\frac{r}{r_x})^{\beta}} \tag{34 a}$$

$$T_e\,(r) = \frac{T_e\,(o)}{1 + (\frac{r}{r_T})^{\tau}} \tag{34 b}$$

and using the integration method described in /27/. (equation (3) in /27/).

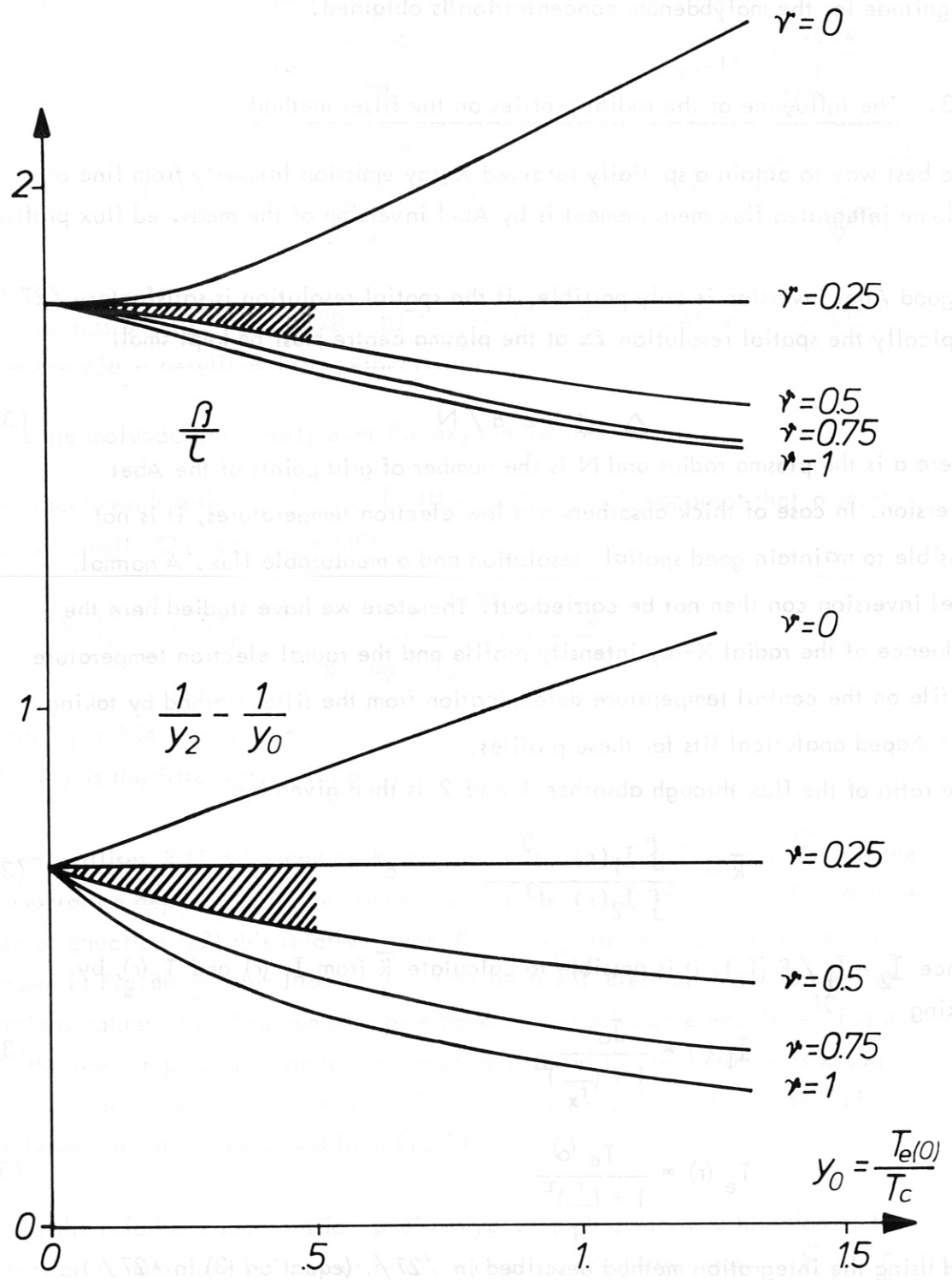

Fig.22 The dependence of $ß/\tau$ and $1/y_2 - 1/y_o$ on y_o. These parameters give the relation between the electron temperature radial profile and the calculated X-ray intensity radial profile for various electron density radial profiles (υ).

This type of radial profile was suggested by H. Wobig and successfully used to fit the data of the W VII A Stellarator (see also section 6.2).

The relative error in the central electron temperature, ε_T, when taking $\bar{R}$ instead of R, is calculated accordingly:

$$\varepsilon_T = \left[\frac{A/T_c}{T_e(o)/T_c} \cdot \frac{1}{(\ln \bar{R})^{1/\alpha}} \right] - 1 \qquad (35)$$

Note that ε_T is a function of the parameters: $\beta, \tau, r_x, r_T, A/T_c, T_e(o)/T_e$ defined in equations (25), (26) and (34).

It is clear that there are too many parameters to treat as variables in order to study their influence on the line of sight integration. However most of these parameters are interdependent. We will derive the dependence of β on τ and r_x on r_T and further use general experimental facts to further reduce the number of free parameters for the error ε_T.

The interdependence of the parameters will be derived for a plasma in coronal equilibrium and with a homogeneous oxygen concentration given by $n_z \overline{Z} \backsim n_e$.

Firstly a relation between r_x and r_T is found:
Starting from equation (25) and taking $n_e(r) \propto T_e(r)^{\nu}$ the local intensity is given by

$$I(r) = C \; T_e^{2\nu - 1/2} \; e^{-T_c/T_e} \qquad (36)$$

with T_e a function of r, given by (34 b). Hence the broadness of the X-ray profile $r_2(I) = r_x$ is related to $r_2(T_e) = r_T$ as:

$$\left(\frac{r_x}{r_T}\right)^{\tau} = y_o \left[\frac{1}{y_2} - \frac{1}{y_o} \right] \qquad (37)$$

with y_o, y_2 the normalised temperatures at $r = o$ and $r = r_x$: $y_o = T_e(o)/T_c$; $y_2 = T_e(r_x)/T_c$

y_2 is obtained from (36) accordingly:

$$y_2^{2\nu - 1/2} \; e^{-1/y_2} = 1/2 \, y_o^{2\nu - 1/2} \; e^{-1/y_o}$$

Fig. 22 shows $1/y_2 - 1/y_o$ plotted versus y_o for various density profiles.

Secondly a relation between β and τ is found: If we normalize r by putting $= (r/r_x)^{\tau}$,

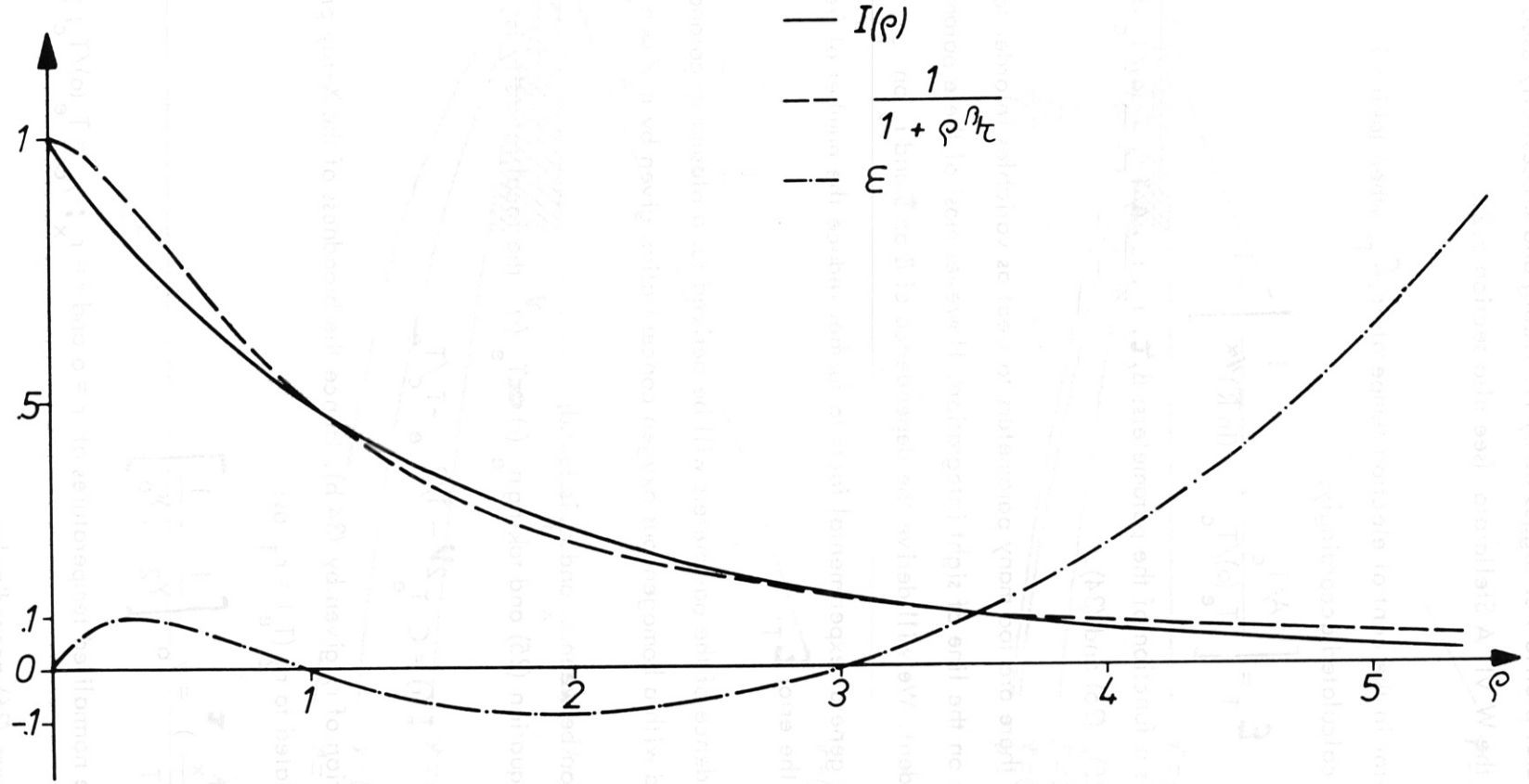

Fig.23 Comparison between the calculated X-ray intensity radial profile I (ρ) (-line) and the best fit (--line). Showing the relative error ε as a function of $\rho = (\frac{r}{r_x})^{\tau}$ (- · - line)

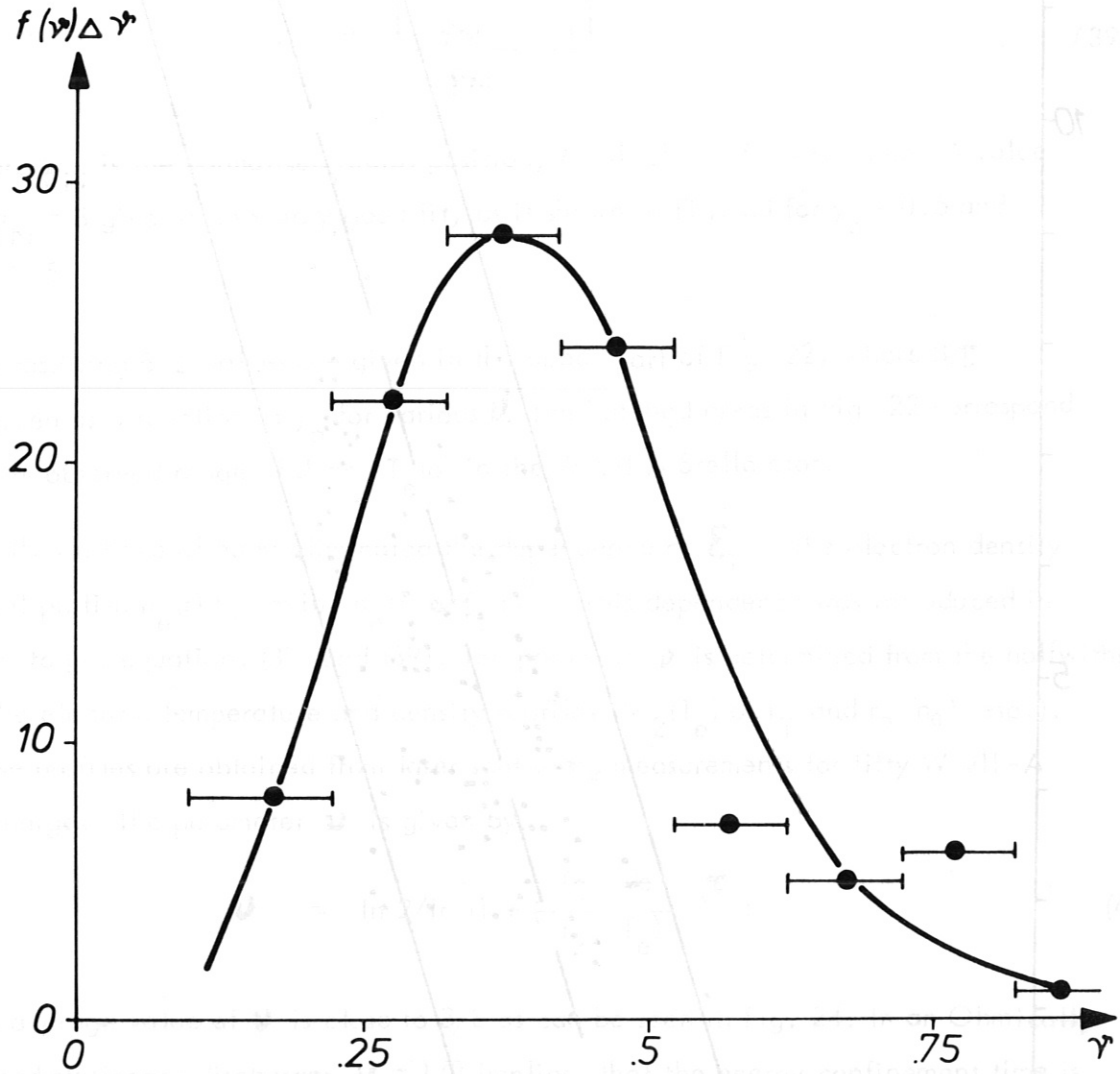

Fig.24 The observed distribution $f(\upsilon)$ for W VII-A discharges. The parameter relates the electron density radial profile with the temperature profile: $n_e(r) \propto T_e(r)^{\upsilon}$

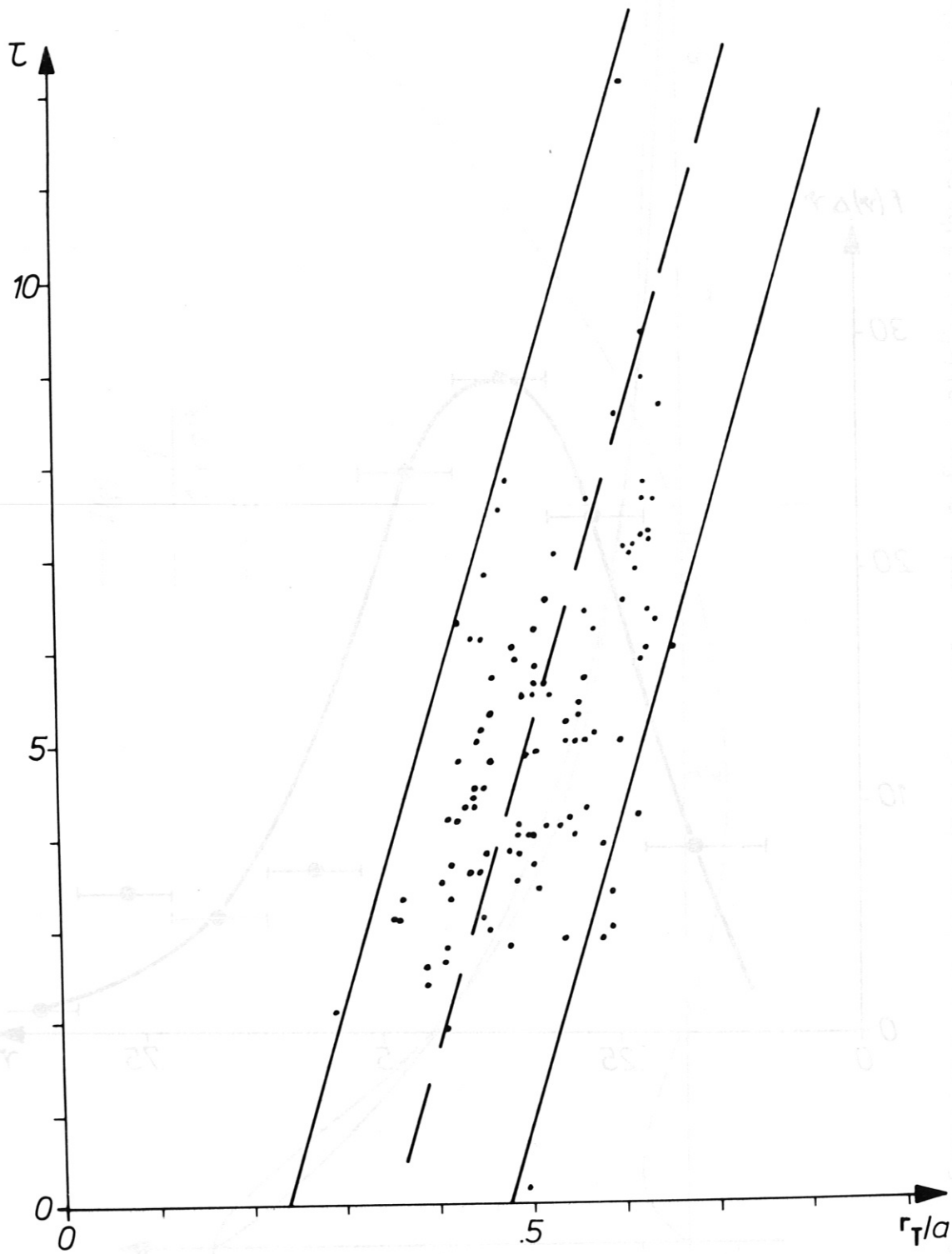

Fig.25 The observed relationship between the steepness τ and the broadness r_T of the electron temperature radial profile in W VII-A (a is the plasma radius).

equation (36) can be rewritten, with I normalized in the centre, as

$$I(\rho) = 1 + \rho\, y_o \left(\frac{1}{y_2} - \frac{1}{y_o}\right)^{-(2\nu-1/2)} e^{-\left(\frac{1}{y_2} - \frac{1}{y_o}\right)\rho} \qquad (38)$$

The dependence of ß on τ is obtained by fitting the hyperbolic like function given by (34 a) to the function given by equation (38). It follows that

$$\frac{ß}{\tau} = \frac{\ln\left[I(\rho_N)^{-1} - 1\right]}{\ln \rho_N} \qquad (39)$$

where ρ_N is the normalised radial position, at which the fit was taken. A value of $\rho_N = 3$ gives a rasonably good fit, as is shown in Fig. 23 for $y_o = 0.5$ and $\nu = 0.5$.

The resulting $ß/\tau$ values are given in the upper part of Fig. 22, where $ß/\tau$ is given as a function of y_o for various ν. The hatched areas in Fig. 22 correspond to the observed range of ν and $T_e(o)$ in the W VII A Stellarator.

Thirdly we have already eliminated the dependence of ε_T on the electron density radial profile $n_e(r)$ by taking $n_e(r) \propto T_e(r)^{\nu}$. This dependence was introduced in order to get equations (37) und (39). The parameter ν is determined from the halfwiths of the electron temperature and density profiles ($r_2(T_e)$ or r_T and $r_2(n_e)$ resp.). These profiles are obtained from laser scattering measurements for fifty W VII-A discharges. The parameter ν is given by:

$$\nu = \ln 2 / \ln\left(1 + \left(\frac{r_2(n_e)}{r_2(T_e)}\right)^{\tau}\right) \qquad (40)$$

The average value of ν is close to 3/8 as can be seen in Fig. 24. In an Ohmically heated stationary discharges, $\nu = 1/2$ implies, that the energy confinement time is constant over the radius /15/.

Fourthly we now eliminate the dependence of ε_T on $r_2(T_e)$ or r_T. An experimental relationship has been found between $r_2(T_e)$ and the steepness τ (see Fig. 25). The uncertainty in this relation shown in the figure causes the spread in the correction ε_T as indicated in tabel II.

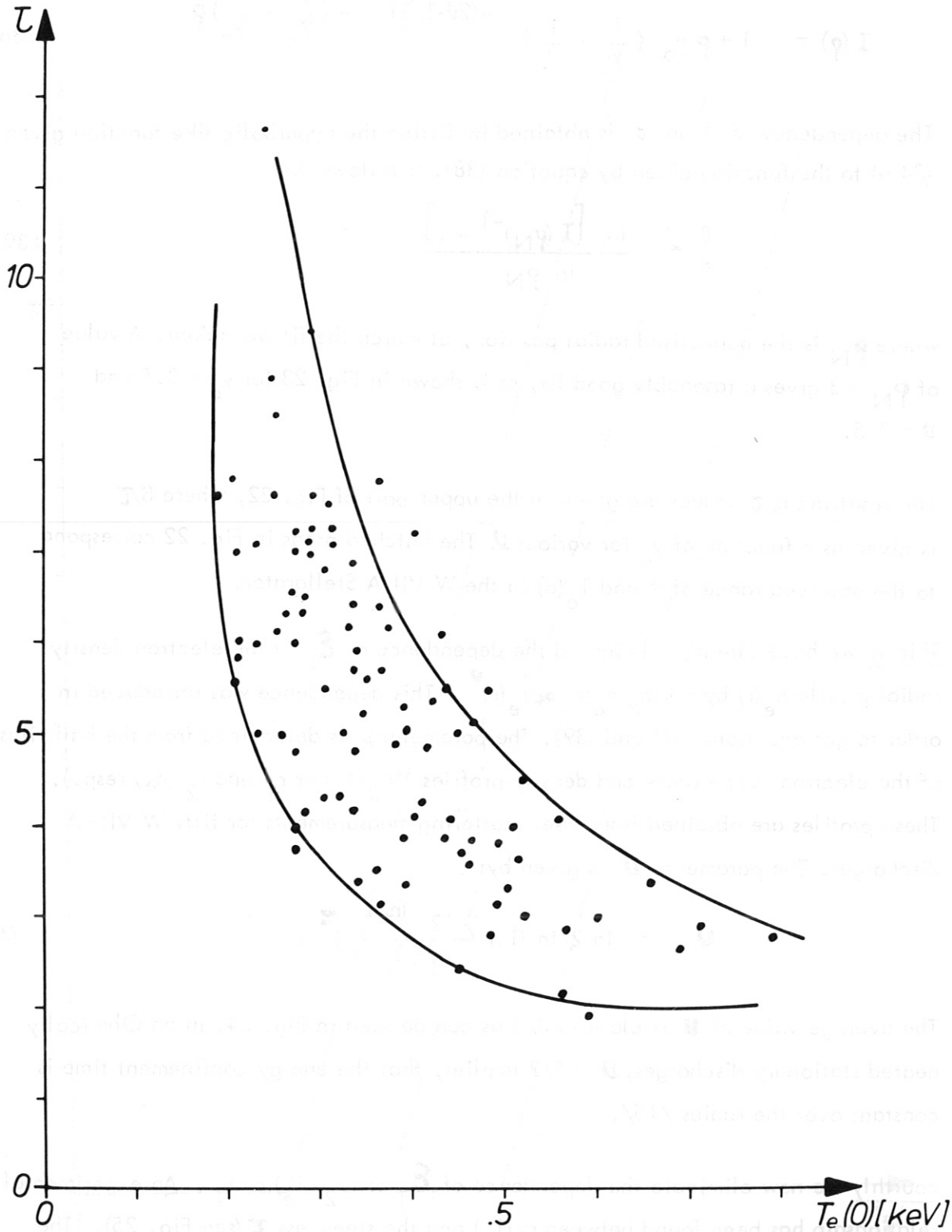

Fig.26 The relationship between the steepness τ of the $T_e(r)$ profile and the central electron temperature observed in W VII-A.

The solid lines in Fig.25, enveloping the measured points, are used to give the required connection between r_T and τ. Using equations (39), (37), (35), (33) the relative error ε_T is calculated as a function of $y_o = T_e(o) / T_c$ and τ. The results are shown in table II.

TABLE II

τ \ y_o	.1	.2	.3	.4	.5
2	$-.103 \pm .020$	$-.139 \pm .020$	$-.175 \pm 0.26$	$-.202 \pm .029$	$-.227 \pm .033$
3	$-.050 \pm .006$	$-.082 \pm .010$	$-.109 \pm .017$	$-.132 \pm .021$	$-.152 \pm .025$
4	$-.032 \pm .003$	$-.056 \pm .097$	$-.077 \pm .011$	$-.097 \pm .012$	$-.111 \pm .017$
5	$-.024 \pm .003$	$-.042 \pm .005$	$-.059 \pm .008$	$-.073 \pm .011$	$-.087 \pm .013$
6	$-.019 \pm .002$	$-.034 \pm .004$	$-.047 \pm .006$	$-.060 \pm .008$	$-.071 \pm .010$
7	$-.015 \pm .001$	$-.028 \pm .003$	$-.038 \pm .003$	$-.048 \pm .005$	$-.062 \pm .008$

Relative error ε_T in $T_e(o)$ for $\frac{A}{T_c} = .415$.

The value shown for each ε is approximately that calculated for the broken line in Fig.25 and for $\upsilon = 3/8$. The plus and minus variations in ε are obtained from the left and right full lines in Fig.25 with either $\upsilon = 1/4$, 1/2 or 3/4. The variation in the error is mainly dependent on the parameter r_T/a.

The tabel II is rather general, because variations of the filter combination-parameter A/T_c from 0.4 to 1.0 diminishes ε_T only by 10 %. The ε values in tabel II can be approximated by an analytic expression

$$\varepsilon (y_o, \tau) = -0.64 \; y_o^{0.38} \; \tau^{\frac{-0.94}{y_o 0.2}} \qquad (41)$$

The steepness τ can either be obtained from measured electon temperature profiles or from the Abel inverted X-ray profiles, measured through thinner filters according to the upper part of Fig. 22. In an iterative way the correct electron temperature can then be obtained from the filter method temperature (eq. 27).

Finally, in order to enable a time resolved on-line computation of the central electron temperature after each discharge, a rough experimental relationship found between the steepness τ and T_e (o) is used (see Fig. 26). This relationship is an inreasing steepness τ with a decreasing T_e(o). It is due to an expanding radius of $q = 1$ with increasing density and increasing external rotational transform ι_o,

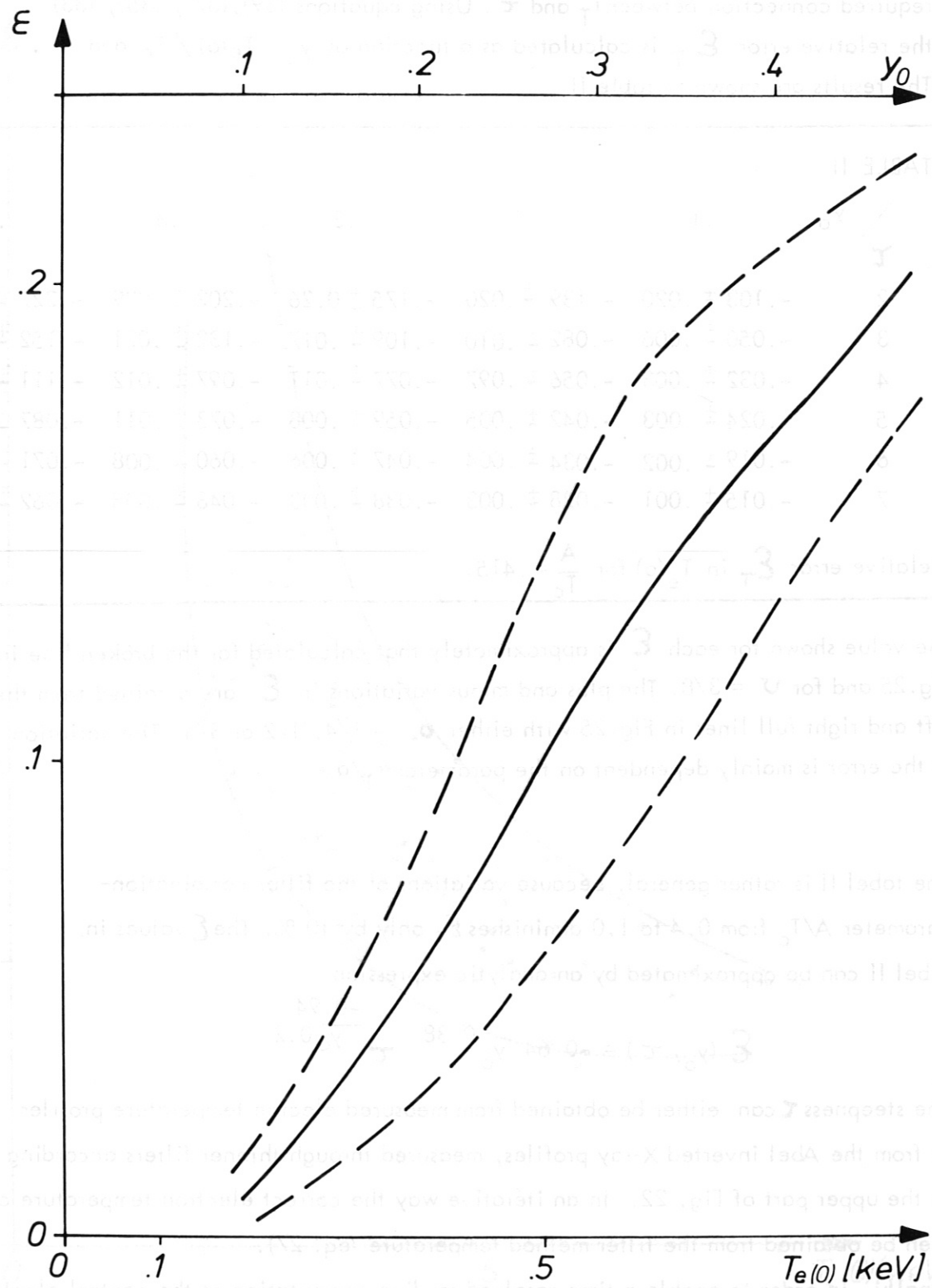

Fig.27 The relative error (or correction) in T_e as a function of T_e (o) or y_o due to the radial profiles. The uncertainty (broken lines) is due to the spread in τ for a given T_e(o).

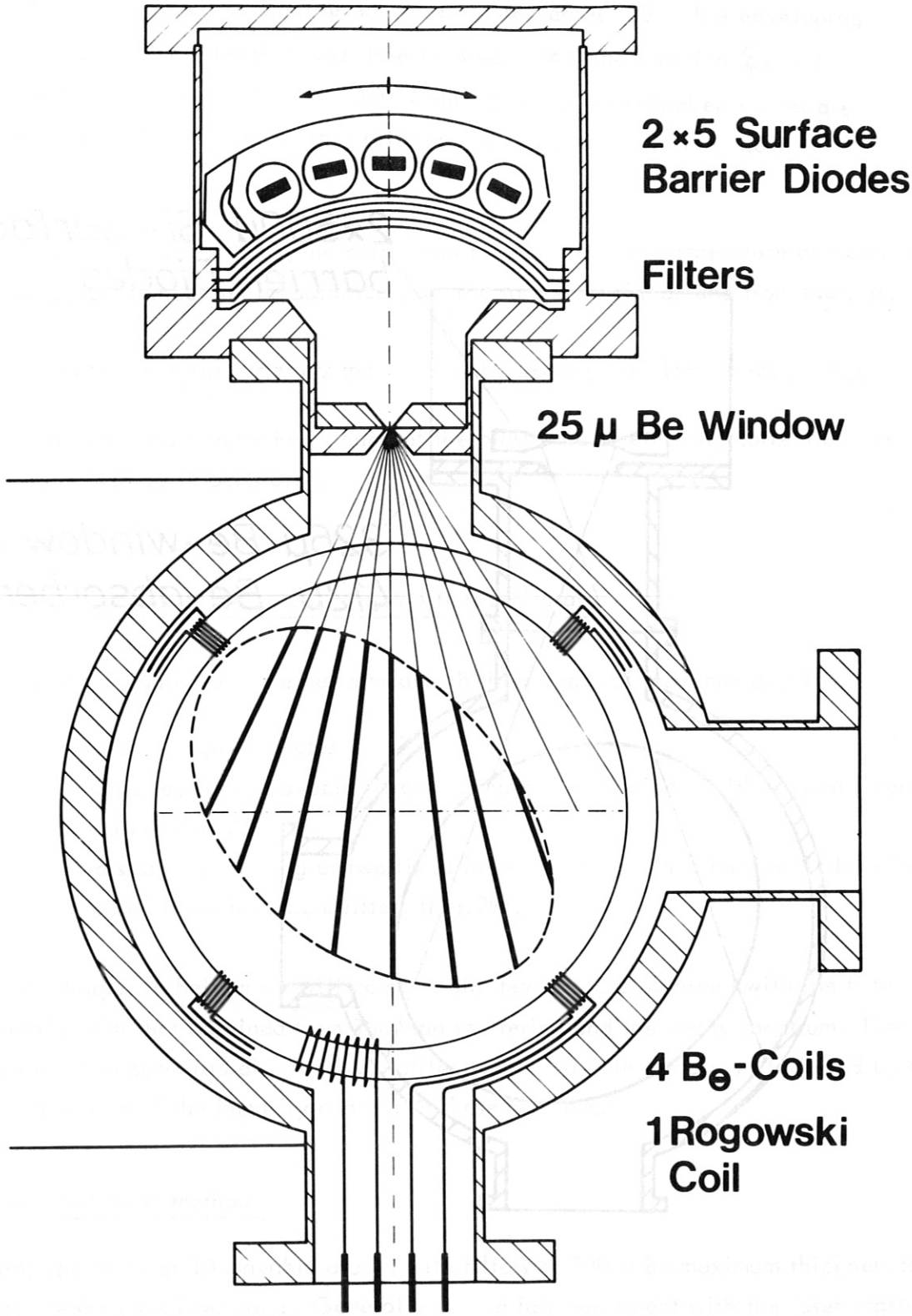

Fig.28 The X-ray pinhole camera installed in the W VII-A Stellarator.

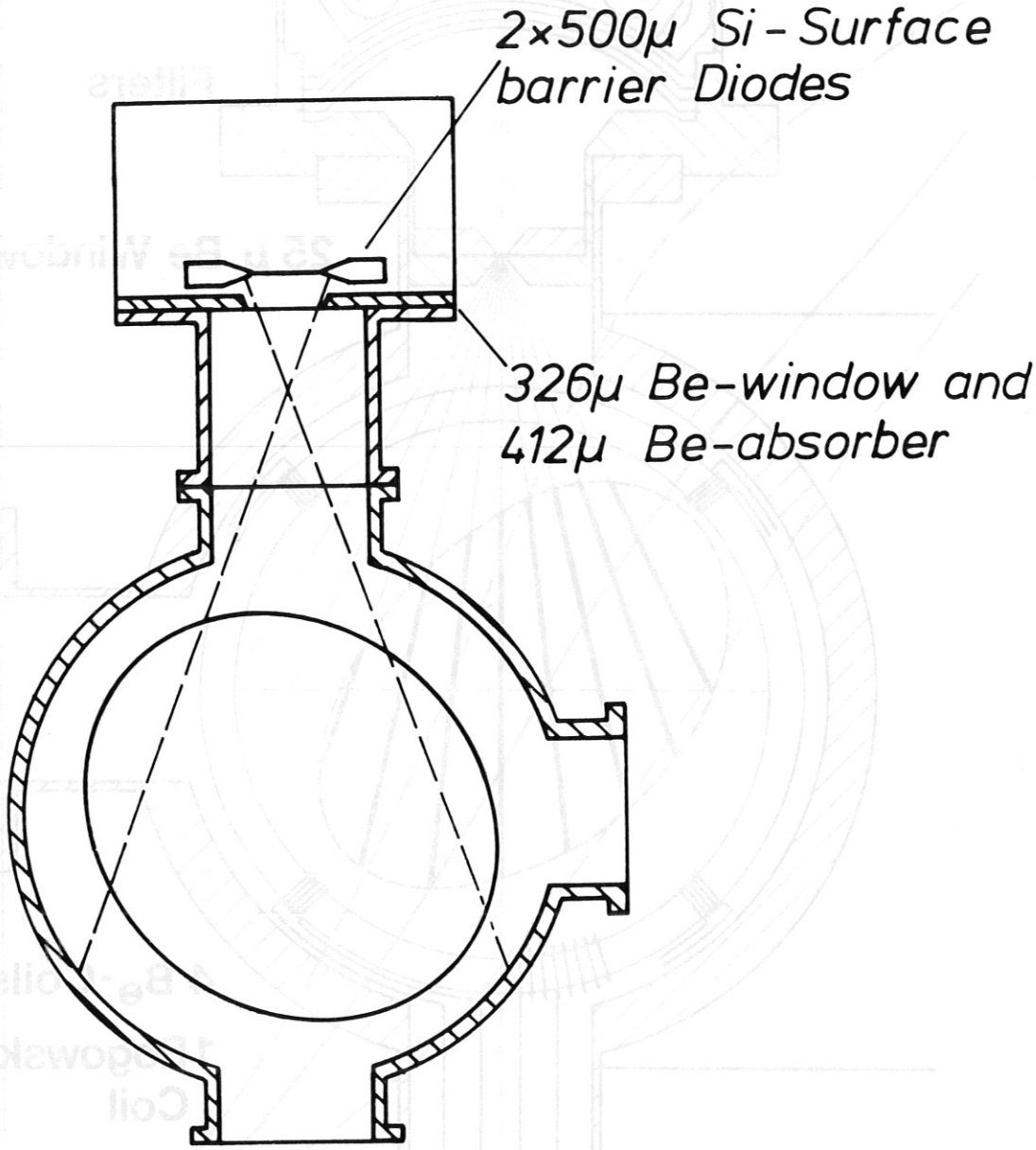

Fig.29 Sketch of the thick filter X-ray flux detector system.

in both cases the central electron temperature decreases /29/. The enveloping curves in Fig. 26 are used to calculate from eq . (41) the function $\mathcal{E}_T(y_o)$. The results are shown in Fig. 27, where the upper an lower broken curves are obtained from the lower and upper solid curves respectively in Fig. 26.

The maximum uncertainty in the correction for the electron temperature as measured by the filter method can be obtained from the spread in Fig.27 and from table II.

For example: at $T_e(o) = 700$ eV the expected correction is -16% (+ 6%, -7%).

So even without a precise knowledge of the plasma parameters the correction can be determined quite accurately.

6. Applications in the case of the W VII A Stellarator

The X-ray measurements are performed with three types of instruments: /23/

- a Si (Li) spectrometer
- an array of 10 movable silicon surface barrier diodes with several insertable filters (Fig.28)
- a system consisting of two fixed large silicon surface barrier diodes with fixed thick beryllium filters (Fig.29).

For discharges in helium we will compare the temperature obtained with the filter method, with that obtained from Thomson scattering and the X-ray spectrum. Then we will show some radial intensity profiles, obtained with the array, followed by the determination of the impurity content in these discharges.

6.1. The filter method

Using the array of 10 movable diodes with filters of 300 μ Be maximum thickness the filter method has been used. Generally a fair agreement with the laser scattering temperature was found. But the thinner filters (50 μ Be) are then still perturbed by the stainless-steel L-lines. (When present the fluxes through both filters are influenced by the molybdenum L-lines).

Also the thin filter measurements are dependent on the shape of

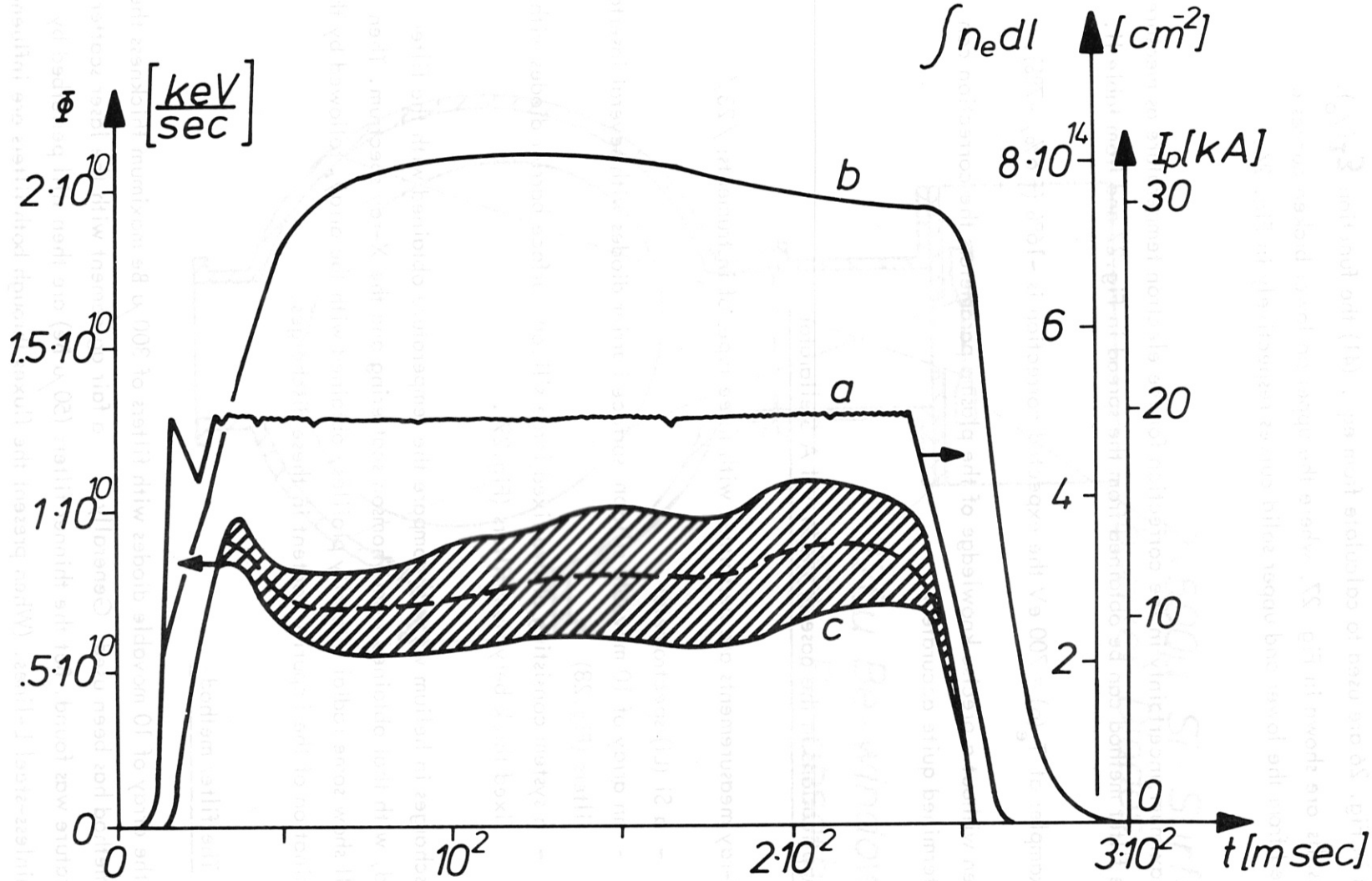

Fig.30 Time history of plasma current I_p (trace a), electron density $\int n_e dl$ (trace b) and the soft X-ray flux Φ (trace c) through 326 μ beryllium for shots 13550 - 13593; $B_o = 3.5$ T; $\epsilon_o = 0.14$; helium.

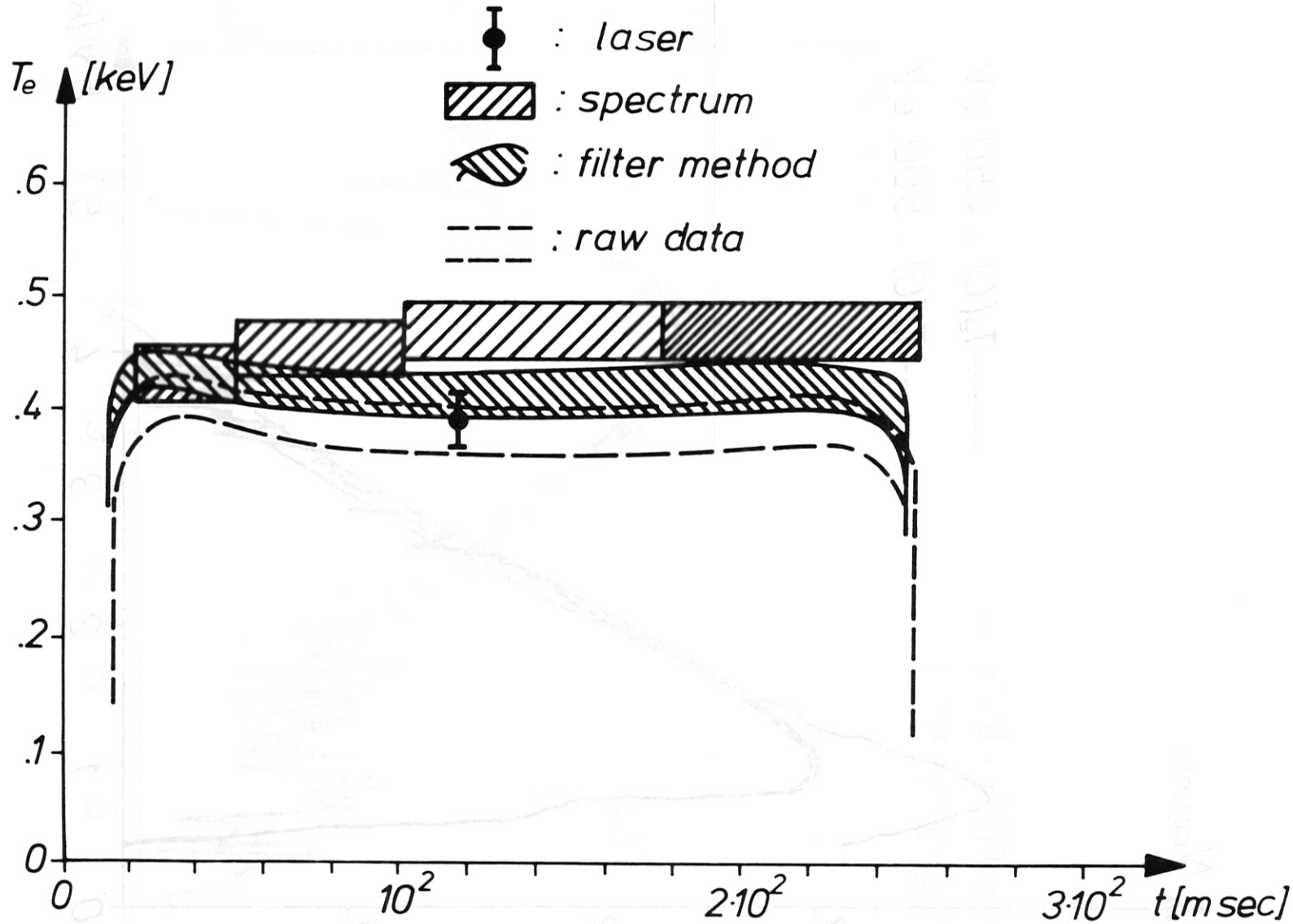

Fig.31 The time history of the central electron temperature for the shots shown in Fig.30, as obtained from laser scattering (one point), the X-ray spectrum, the filter method with and without radial profile corrections.

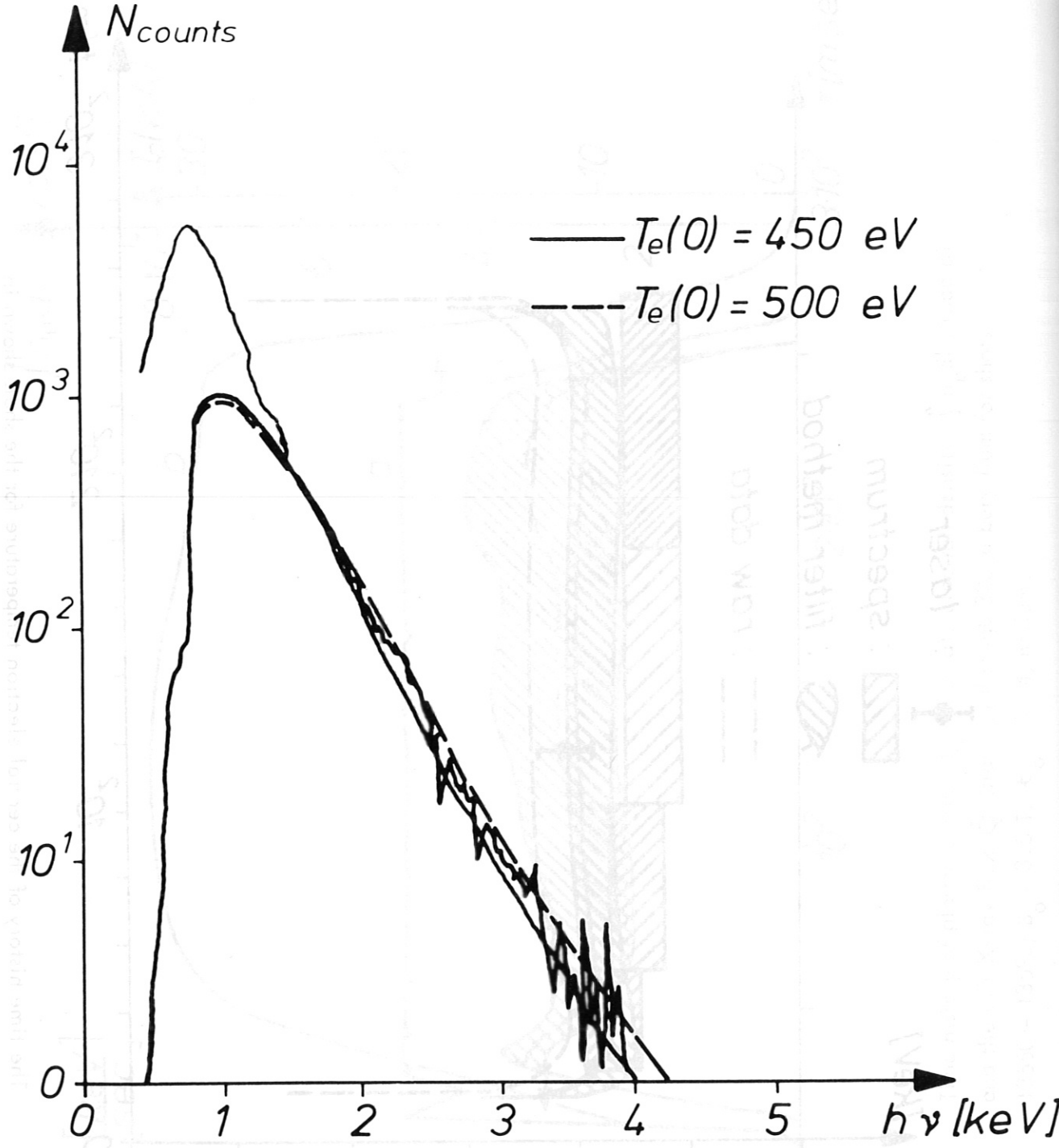

Fig.32 The measured X-ray spectrum between t = 175 and 250 msec for the shots in Fig.30 through 9 μ beryllium. The spectra calculated for oxygen from the electron temperature and density radial profiles for $T_e(o)$ = 450 resp. 500 eV are shown in the figure. The spectra are normalised at $h\nu$ = 2 keV.

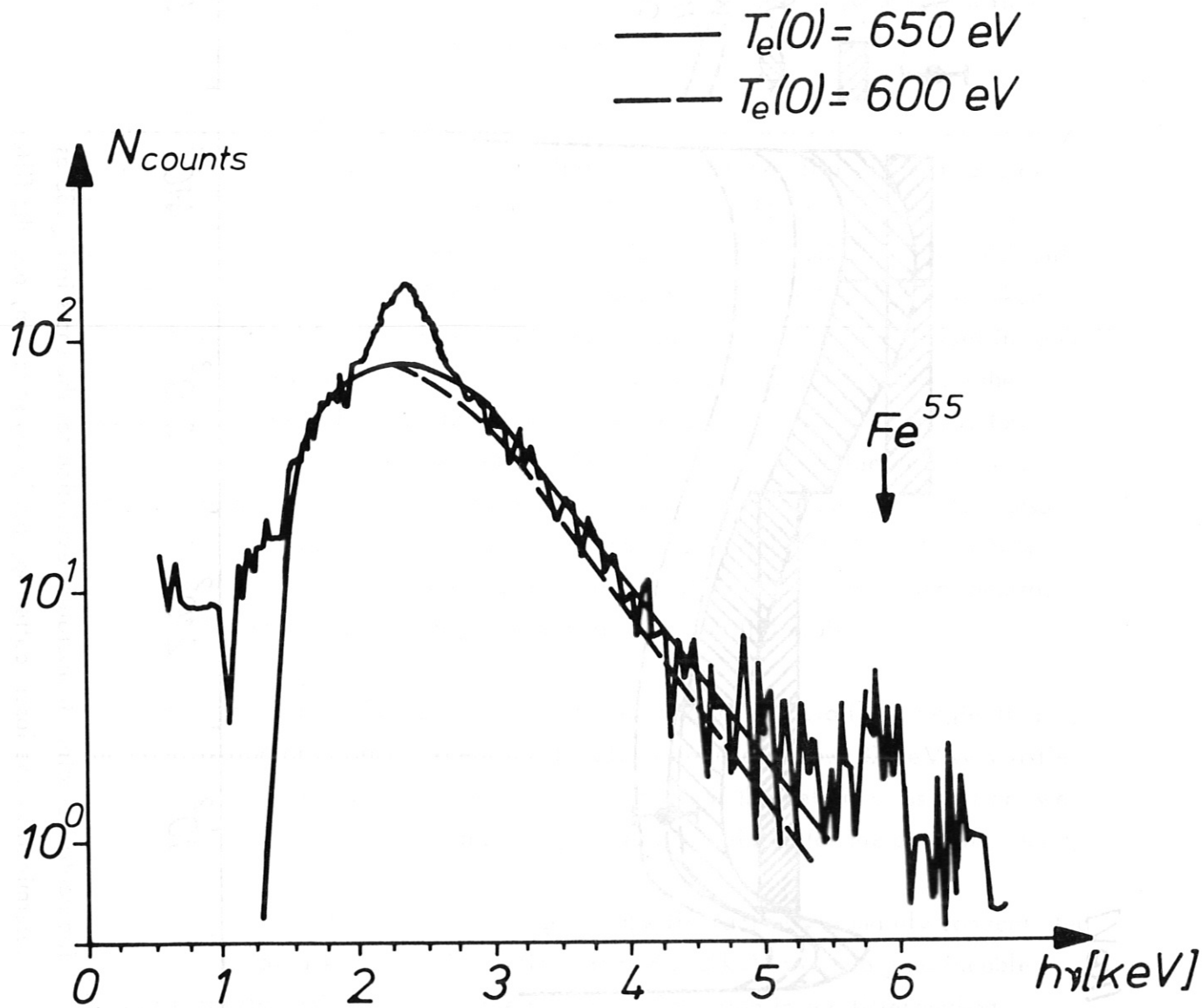

Fig.33 Measured and calculated X-ray spectra at a higher electron temperature through 164 μ beryllium for shots 15162 - 15174 and t = 60 - 160 msec; $B_o = 3.5$ T; $\tau_o = 0.14$; $I_p = 20$ kA; $\int n_e dl = 4 \cdot 10^{14} cm^{-2}$.

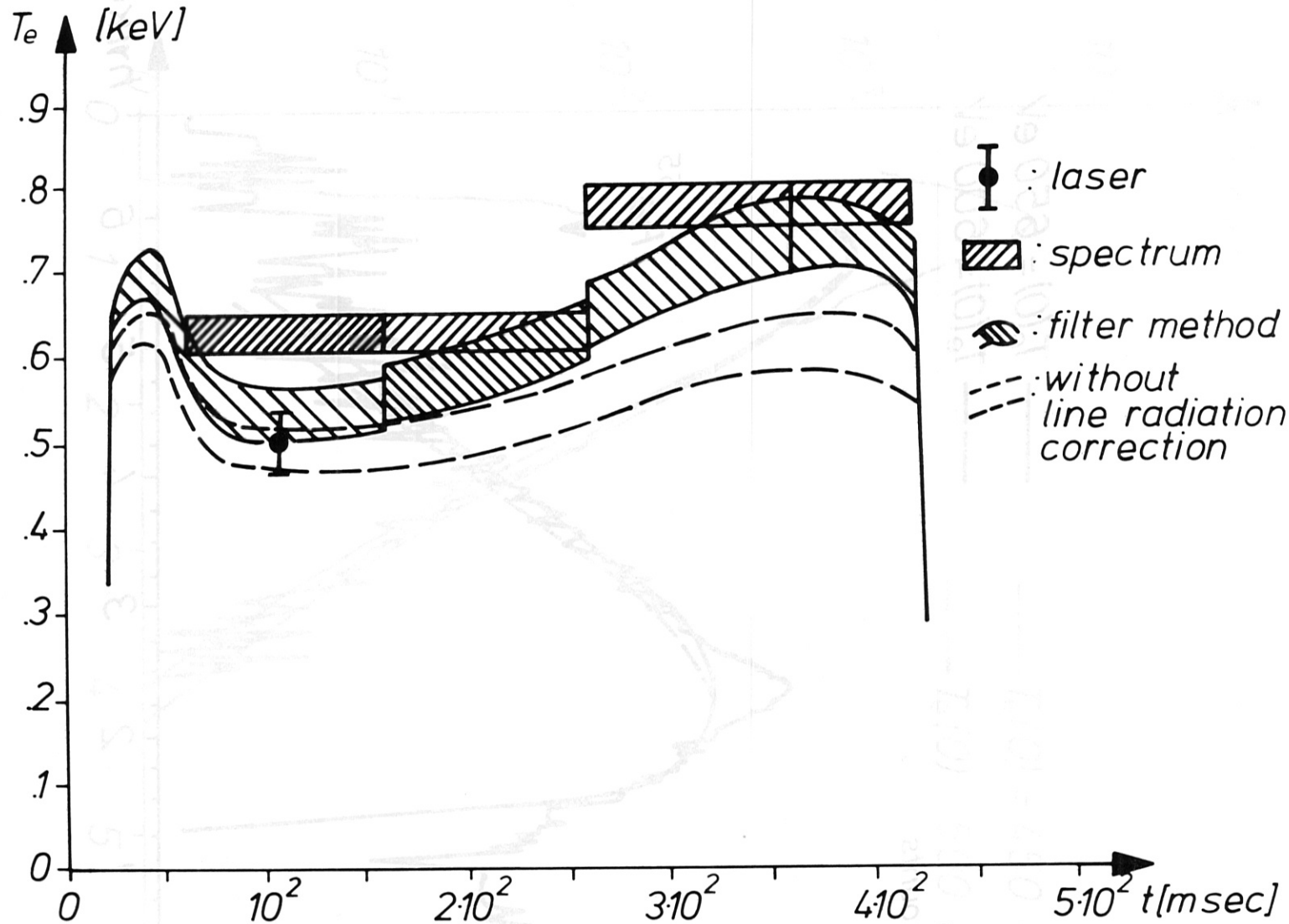

Fig.34 The central electron temperature evolution for the shots in Fig.33 as determined by the laser scattering, the X-ray spectrum, and the filter method with and without line radiation correction.

the radial profile. This can be deduced from table II since a thinner filter implies a higher y_o value for a given electron temperature.

Thus a system with thick beryllium filters was designed in order to cut away the spectrum with energies equal or lower than the molybdenum L-lines and to reduce the influence of the shape of the radial profile.

The spatial resolution had to be sacrified in order to compensate the loss of flux through the thicker filters. The results are shown in the following figures.

Fig.30 shows the time history of the plasma current (trace a), electron line density (trace b) and the soft X-ray flux through a 326 μ thick beryllium filter (trace c). The corresponding electron temperature is given in Fig.31. The raw data of the filter method (trace a) is corrected for the influence of the radial profiles with aid of table II. The steepness τ of the electron temperature radial profile is taken as constant, found from the laser scattering measurements. The mean values in table II were taken. The temperature from the X-ray spectrum (Fig.32) is given by the rectangular boxes in Fig.31. The correct temperature lies more towards the lower side of the box, as can be seen from the Fig.32. The central value of the electron temperature obtained at $t = 100$ msec by the laser scattering measurements is also indicated in the Fig.31. The filter method temperature seems to be only slightly higher. The spectral temperature has been obtained by fitting calculated spectra, including the effects of the temperature and density radial profile.

Oxygen in coronal equilibrium is taken for the spectral calculations, neglecting the contribution of helium. Except for the discontinuities below 870 eV very little difference in the shape of the spectrum would occur if the helium cross sections were included. The filter characteristic $R(T_e)$ is also calculated for the oxygen impurity.

As can be seen from the spectrum in Fig.32, the line activity is mainly concentrated around and below 1 keV. The Mo-L lines around 2.3 keV are hardly noticeable. This justifies the omission of the line radiation correction in the filter method.

At lower densities and therefore higher temperatures the molybdenum L-lines become more pronounced (Fig.33). A correction has then to be made in the filter method. This is shown in Fig.34. The broken lines show the evolution of the electron temperature with radial profile corrections only. The rectangular hatched blocks give the electron temperature obtained over twelve discharges from the X-ray spectrum. The same

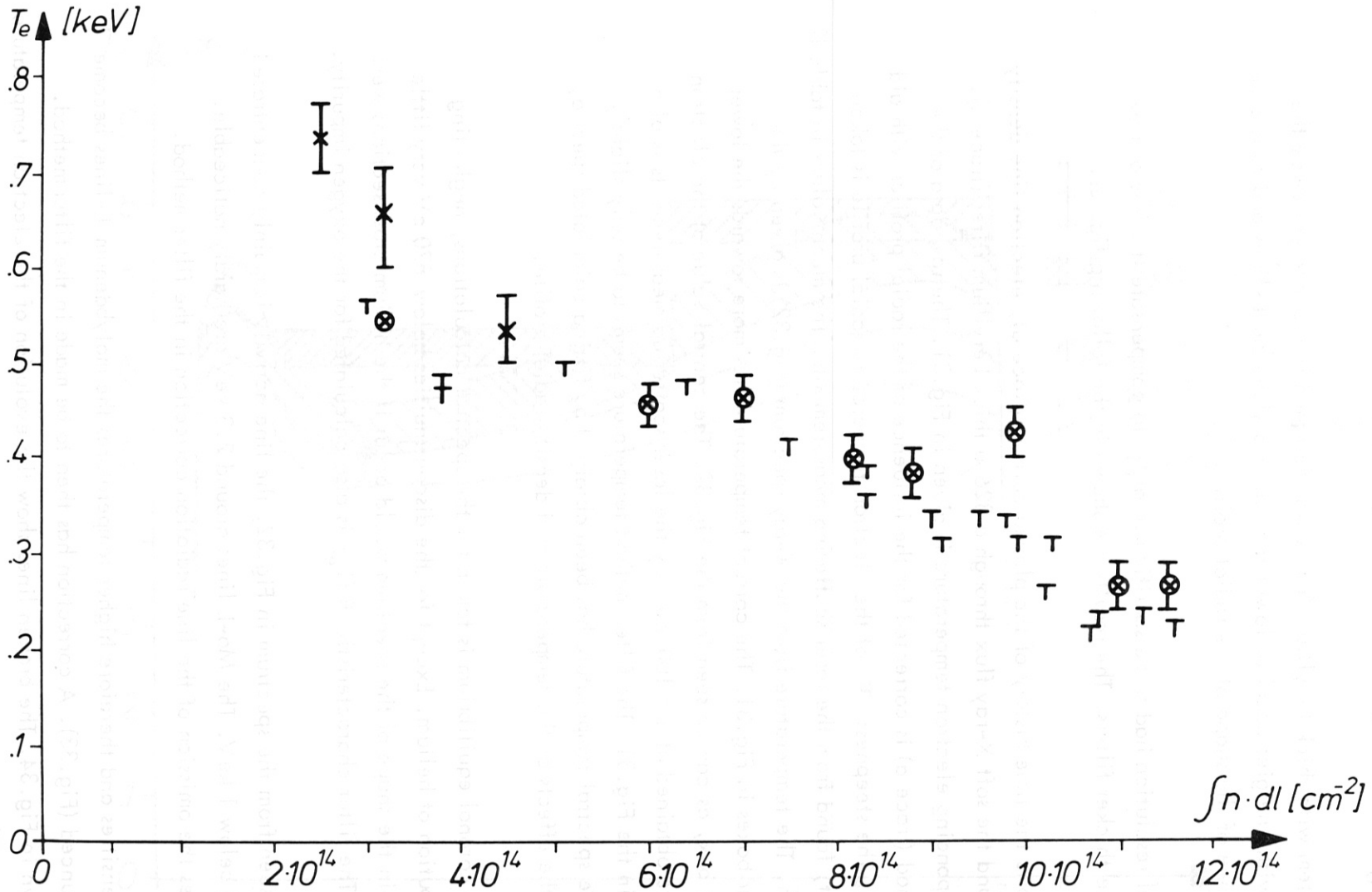

Fig.35 Comparison between the values of the central electron temperature obtained by laser or Thomson scattering (T) and by filter method (X : with radial profile and line radiation corrections) (⊗ : with only radial profile corrections) as a function of $\int n_e dl$; $B_o = 3.5$ T; $I_p = 20$ kA; $\epsilon_o = 0.14$.

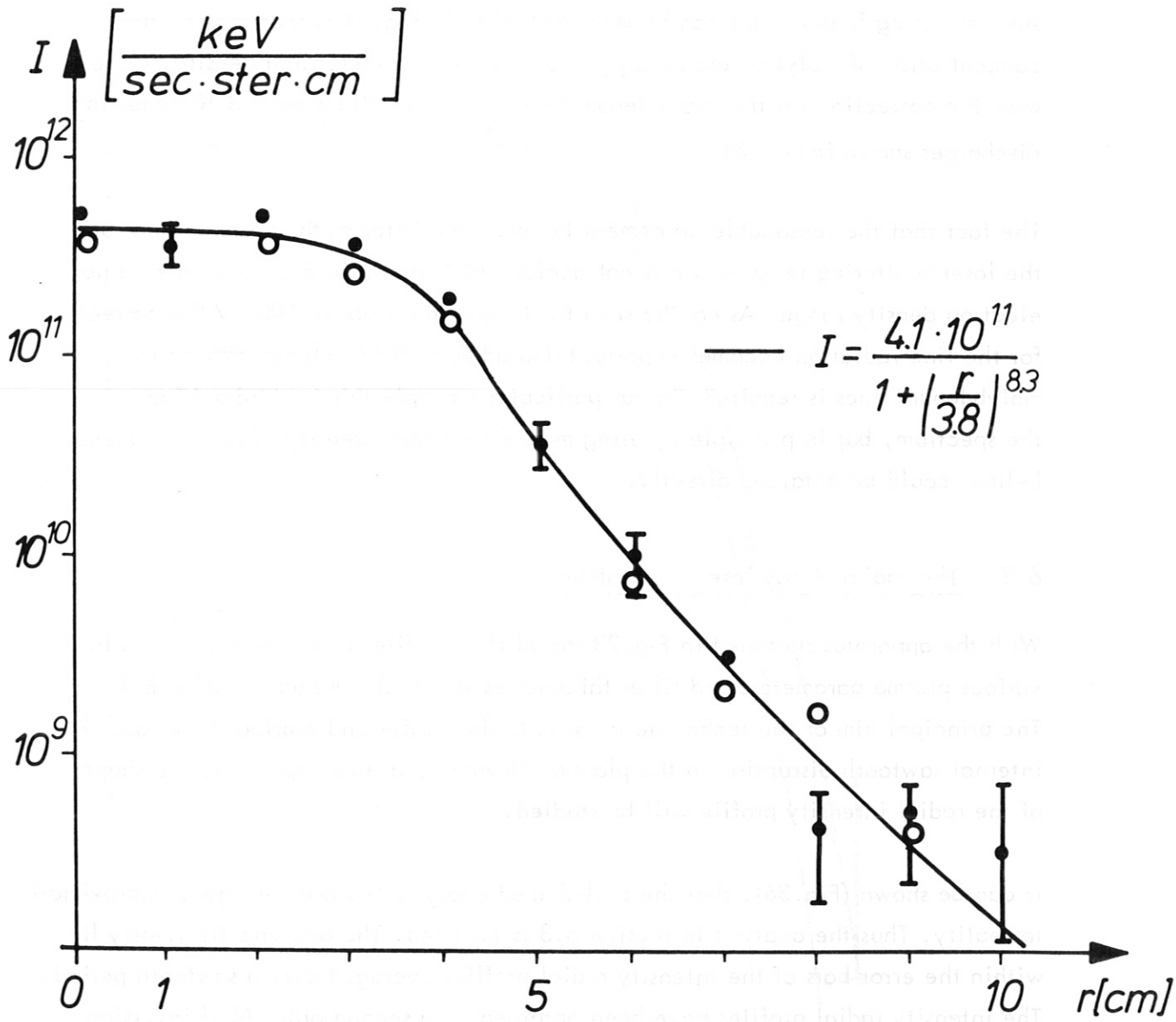

Fig.36 The observed X-ray intensity radial profiles before (●) and just after (o) an internal sawtooth disruption for the shots of Fig.30 through a 25 μ thick beryllium filter at t = 100 msec. A bell-shaped and analytic fit to the average values has been made.

four spectra yield the ratio of the Mo-L-lines over the continuum. This ratio is then used to correct for the molybdenum line radiation in the filter method (the four other hatched areas in Fig.34). The concentration of the molybdenum relative to the concentration of oxygen necessary to explain this correction is around $5 \cdot 10^{-3}$, this can be deduced from Fig.21.

An interesting feature that can be seen with aid of Fig.21 is that the relative concentration of molybdenum to oxygen decreases with increasing density. Otherwise the correction for the molybdenum L-lines would still be around 10 % for the discharges shown in Fig. 31.

The fact that the reasonable agreement between the filter method temperature and the laser scattering temperature is not accidental is shown in Fig.35 over a larger electron density range. As can be seen for temperatures above 500 eV the correction for the line radiation becomes important and additional knowledge about the molybdenum lines is required. In our particular example this is obtained from the spectrum, but in principle by using more filters the intensity of the molybdenum L-lines could be obtained directly.

6.2. The radial X-ray intensity profiles

With the apparatus sketched in Fig.28 radial flux profiles have been measured for various plasma parameters and filter thicknesses (from 25 μ Be up to 300 μ Be). The principal aim of the technique is to study the MHD- and tearing modes and the internal sawtooth disruption in the plasma. However, in this paper only the shape of the radial intensity profile will be studied.

It can be shown (Fig.36), that the bell-shaped analytic fits are very good approximations to reality. Thus the analysis in section 5.3 is justified. The analytic fit usually lie within the error bars of the intensity radial profiles averaged over a sawtooth period. The intensity radial profiles have been obtained by a second order Abel inversion routine including the spatial resolution of the detector system /27/. Because the spatial resolution is about 1 cm, 11 points have been taken for the Abel inversion.

The particular profile shown in Fig.36 was taken through a filter of 25 μ thick beryllium. For other thicknesses (up to 200 μ beryllium) equivalent fits have been made,

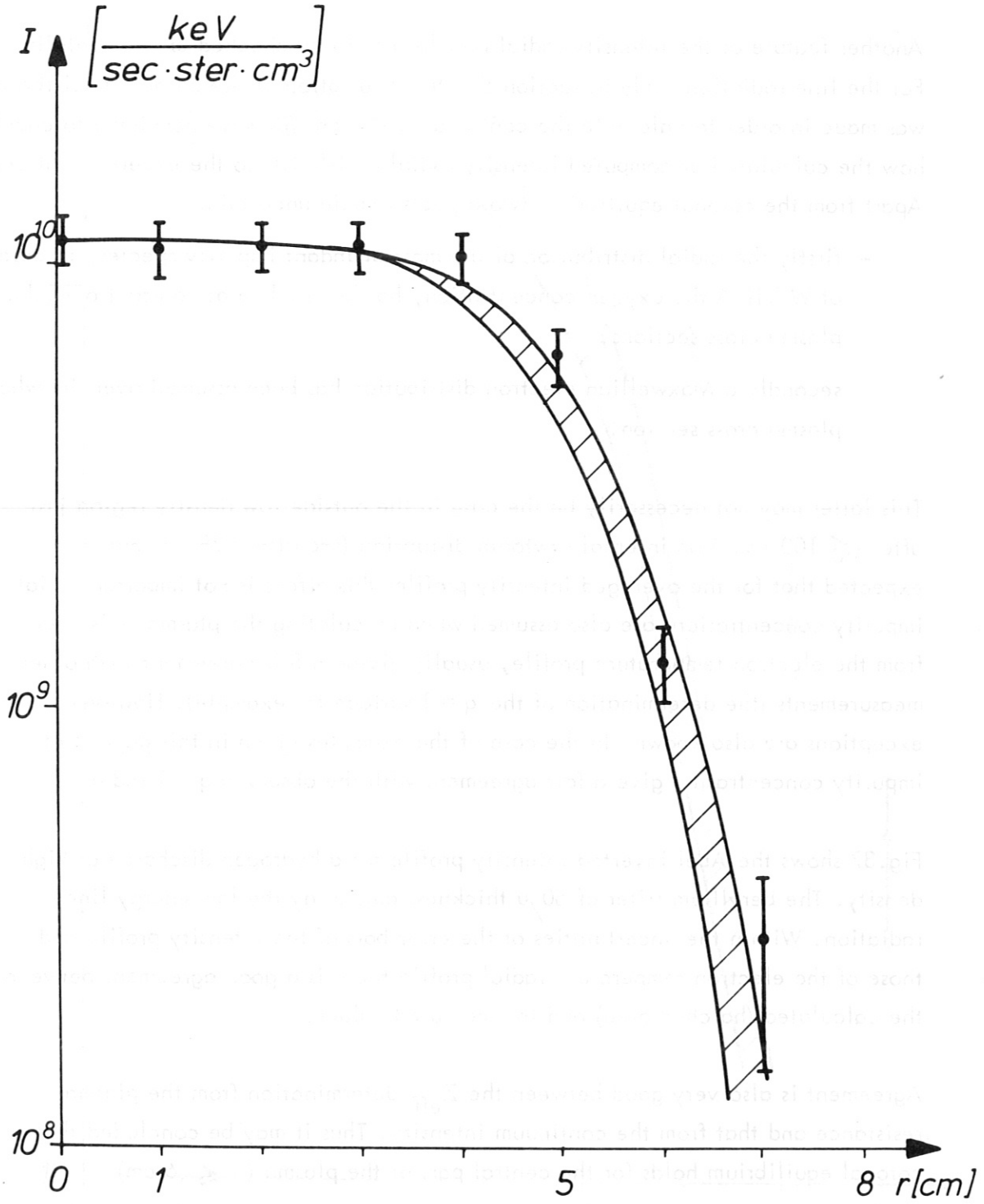

Fig.37 Comparison at higher electron densities of a measured X-ray intensity radial profile and a calculated profile assuming oxygen in coronal equilibrium. (Shots 7986 - 8004: $B_o = 3.0$ T; $\epsilon_o = 0.23$; $T_e(o) = 300$ eV; $n_e(o) = 3.5 \cdot 10^{13}$ cm^{-3}; $Z_{eff} = 1.2$; 50 μ Be).

however not as far to the outside of the plasma as in Fig.36, due to the higher cut off energy of the thicker filters.

Another feature of the intensity radial profiles has to be checked experimentally. For the line radiation study in section 5.2 the assumption of the coronal equilibrium was made in order to calculate the continuum emission. Thus we now have to check how the calculated or computed intensity radial profile fits to the experimental one. Apart from the coronal equilibrium two aspects remain uncertain:

- firstly the radial distribution of the most abundant impurity species, in case of W VII-A the oxygen concentration, has been taken as constant over the plasma cross sections;
- secondly a Maxwellian electron distribution has been assumed over the whole plasma cross section.

This latter may not necessarily be the case in the outside low density region just after ($\lesssim$ 100 μsec) an internal sawtooth disruption (see also /28/). But it is expected that for the averaged intensity profiles this effect is not important. Flat impurity concentrations are also assumed when calculating the plasma resistance from the electron temperature profile, usually giving a fair agreement with other measurements (the determination of the $q = 1$ surface for example). However exceptions are also known. In the case of the examples given in this paper flat impurity concentration give a fair agreement with the observed $q = 1$ radius.

Fig.37 shows the Abel inverted intensity profile for a hydrogen discharge at high density. The beryllium filter of 50 μ thickness cuts away the low energy line radiation. Within the uncertainties of the error bars of the intensity profile and those of the electron temperature radial profile there is a good agreement between the calculated (hatched area) and the measured values.

Agreement is also very good between the Z_{eff} determination from the plasma resistance and that from the continuum intensity. Thus it may be concluded that coronal equilibrium holds for the central part of the plasma ($r \lesssim 6$ cm).

The next example at lower electron density and lower confinement time shows that agreement between the measured and calculated intensity is poor, especially, in the outer plasma region (Fig.38). An enhancement of the radiation as expected

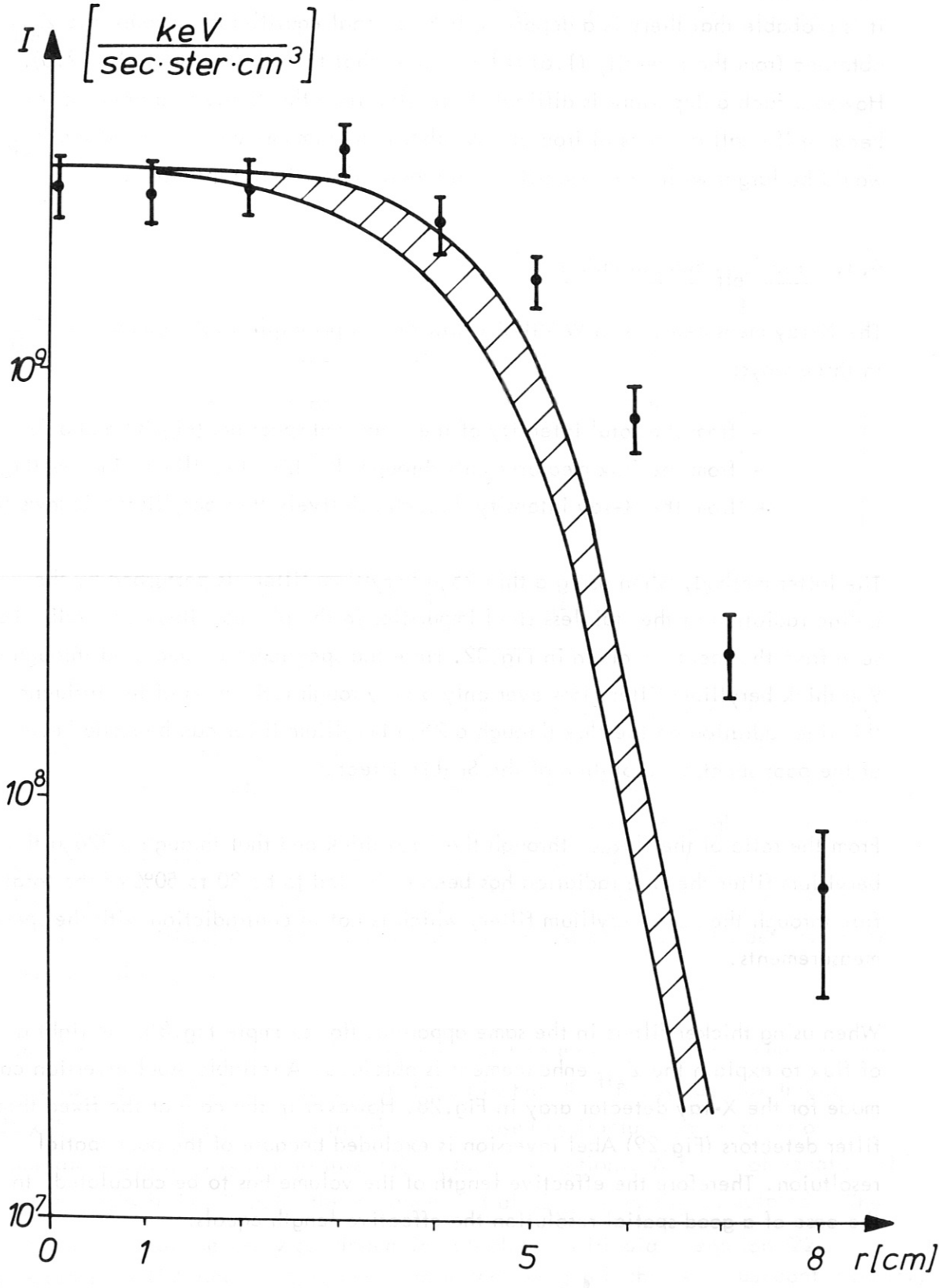

Fig.38 Comparison at lower electron densities of a measured X-ray intensity radial profile and a calculated profile assuming oxygen in coronal equilibrium. (Shots 4465 - 4473, B_o = 3.0 T; t_o = 0.23, $T_e(o)$ = 400 eV; $n_e(o) = 1.4 \cdot 10^{13}$ cm^{-3}; Z_{eff} = 2.0; 100 μ B_e.)

from the outward diffusion of the highly ionised species occurs. Also in the centre it is probable that there is a departure from coronal equilibrium because the Z_{eff} obtained from the intensity (1.6) is lower than that from the conductivity (2.0). However such a departure is difficult to resolve from the X-ray measurements above because if small amounts of iron or any other heavy impurity are assumed the Z_{eff} would be larger without a significant increase of the X-ray intensity.

6.3. The Z_{eff} determination

The X-ray measurements in W VII-A allow one in principle to determine the Z_{eff} in three ways:

- from the total intensity of the measured spectrum (Fig.32 and 33);
- from the flux measurements through the thick beryllium windows (Fig.30);
- from the X-ray intensity through relatively thin beryllium windows (Fig.36).

The latter method, when using a thin 25 μ beryllium filter, is perturbed by the L-line radiation of the stainless steel impurities in the plasma. This can readily be seen from the spectrum given in Fig.32. Here the spectrum was measured through a 9 μ thick beryllium filter. However only a very rough estimation of the influence of this line radiation on the flux through a 25 μ beryllium filter can be made because of the poor spectral resolution of the Si (Li) detector.

From the ratio of the fluxes through the 25 μ thick and that through a 326 μ thick beryllium filter the line radiation has been estimated to be 30 to 50% of the total flux through the 25 μ beryllium filter, which is not in contradiction with the spectral measurements.

When using thicker filters in the same apparatus (for example Fig.35) the right amount of flux to explain the Z_{eff} enhancement is obtained. A reliable Abel inversion can be made for the X-ray detector aray in Fig.28. However in the case of the fixed thick filter detectors (Fig.29) Abel inversion is excluded because of the poor spatial resoltuion. Therefore the effective length of the volume has to be calculated. In the case of a good spatial resolution the effective length equals:

$$\ell_{eff} = c \cdot r_2 \qquad (42)$$

where c is a function of ß (or τ) defined in equation (34).
c is roughly equal to 2.

When the spatial resolution detoriates, c diminishes slightly. This is shown for the thick filter combination in table III.

TABLE III

$\tau \backslash y_o$	0.1	0.2	0.3	0.4	0.5
2	1.3	1.6	1.8	1.9	1.9
3	1.6	1.75	1.85	1.9	1.9
4	1.75	1.85	1.9	1.9	1.9
5	1.85	1.9	1.9	1.9	1.95
6	1.9	1.9	1.9	1.95	1.95
7	1.9	1.9	1.95	1.95	1.95

Normalised effective length $c = \ell_{eff} / r_2$

For this apparatus c is practically a constant (1.8 ± 0.1), so that the determination of r_2 yields the needed central intensity. The radius r_2, where the intensity is half of the central value, is then calculated either from the electron temperature profile (equation 37) or indirectly from the intensity profile measured through thinner filters. Since the agreement between the calculated r_2 and the measured value for the thinner filters is rather good (usually within $\sim$ 10%), the calculated r_2 for the thick beryllium filters should not introduce any important errors in the determination of the central intensity.

In this way the value of r_2 for the discharges indicated in Fig.30 has been estimated to be: $r_2 = 3.4 \pm 0.15$ cm. The hatched area in Fig.30 is the X-ray flux through 326 μ beryllium. The spread in the signal is caused by fluctuations in electron temperature and density due to internal sawtooth disruptions. With aid of equation (17) and the graphs in Fig.2 and 3 the enhancement of Z_{eff} is readily calculated. The enhancement of the x-ray continuum in calculated with aid of eqation (22). We know from UV spectroscopic observation that oxygen is the most abundant impurity, so that the most probable enhancement is $\Delta Z_{eff} \sim 0.2$.

This means an impurity concentration of $n_{oxygen}/n_e \sim 3.5 \cdot 10^{-3}$. If the information about the abundance of oxygen from the UV spectroscopy did not exist, it would have been necessary to include iron and molybdenum in the calculations.

For iron the results would be $\Delta Z_{eff} \backsim 0.7$ and $n_{Fe}/n_e \backsim 3 \cdot 10^{-3}$. The results for molybdenum would lie in between those of oxygen and iron. Obviously from the X-ray flux alone it is not possible to obtain accurate information of the plasma effective charge.

7. Conclusion and discussion

For the W VII-A plasma parameter range it has been shown that the thick filter method is not strongly dependent on the coronal equilibrium condition (Fig.18).

The influence of the radial X-ray intensity and electron temperature profiles had to be calculated, since for the thick filters an Abel inversion was not possible. The correction for the radial profiles (table II) can be kept small by a suitable choice of the thickness of the filters.

A good agreement between the laser scattering, X-ray spectrum and filter method temperature has been found.

At higher electron temperatures a correction for the molybdenum L-line radiation is necessary. The estimated molybdenum concentration is roughly in agreement with that obtained by VUV spectroscopy.

In principle, with the aid of more filters, this line radiation can be eliminated, so that the filter method is still the most appropriate independent electron temperature measurement available with a good time resolution.

Two main points are still uncertain:

- the continuum emission cross sections for multi-electron ions (the non-hydrogenic ion);
- the coronal equilibrium assumption.

In our particular example (W VII-A) oxygen is the most abundant impurity. Therefore it has been impossible to check the approximate cross sections given by equation (3). However in future larger devices the temperature should be much higher, which reduces the importance of oxygen relative to the heavier impurities such as iron and molybdenum (see for instance Fig.2). Therefore, unless more precise calculations are made possible, the emission cross sections remain approximate ($\backsim$ 40%).

In the future in bigger devices the coronal equilibrium condition will be more readily satisfied because of the longer confinement times. However the question of whether coronal equilibrium exists in the outside regions remains of importance. Because of the largely unknown diffusion mechanisms the solution of this problem as given by TFR group (18) seems to be the most promising.

Acknowledgements

The author is grateful to Dr. J. How for carefully reading the manuscript. Many enlightening discussions with Dr. D. Launois and Dr. D. Marty were very helpful in various stages of the work. The X-ray experimental results on the Wendelstein VII-A stellarator were produced together with Dr. A. Weller and with the excellent technical assistance of Mr. D. Gonda and finally with the whole W VII-team.

References

/1/ Equipe TFR: Electron temperature and Z_{eff} measurements in the hot plasma of TFR by soft-X-ray analysis. Nuclear Fusion 17, 2 (1977), 213

/2/ D.A.Marty, P.Smeulders, D.Launois: Description du programme de calcul E.M.X. Etude des Mesures de Rayons X-Mous. EUR-CEA-FC-969, Juillet 1978

/3/ P.Bogen: X-ray diagnostics of plasmas, in plasma diagnostics. W.Lochte-Holtgreven, Editor.

/4 a/ P.J.Brussaard, M.C.van de Hulst : Approximation formulas for nonrelativistic Bremsstrahlung and average Gaunt factors for a Maxwellian electron gas. Rev.Mod.Phys. 34 (1962), 507

/4 b/ W.J.Karzas, R.Latter: Electron Radiative Transitions in a Coulomb Field. Astrophys.J.Suppl. 6 (1961), 167

/4 c/ H.W.Koch, D.W.Motz: Bremsstrahlung Cross-Section Formulas and related Data. Rev.Mod.Phys. 31 (1959) 920

/5/ Wm.J.Veigele, E.Briggs, L.Bates, E.M.Henry, B.Bracewell: X-ray cross section compilation from 0.1 keV to 1 MeV. KN-71-431 (R), 31.July 1971

/6/ TFR Group: Space-Resolved Vacuum Ultraviolet Spectroscopy on TFR Tokamak Plasmas. EUR-CEA-892, April 1977 and Plasma Physics 19 (1977) 587

/7/ S.von Goeler, W.Stodiek, H.Fishmann, S.Grebenshchikov, E.Hinnov: Thermal X-ray Spectra and impurities in the ST Tokamak. MATT 1081, January 1975

/8/ S.Sesnic: Evolution of internal modes, disruptions and high-Z impurities at high density in Pulsator. IPP III/22, April 1976

/9/ M.Mattioli: Revue Bibliographique des Coefficients d'ionisation, de recombinaison et d'excitation des impuretés presentes dans un plasma. EUR-CEA-FC-761, Février 1975

/10/ W.Bambynek, B.Crasemann, RW.Fink, H.U.Freund, H.Mark, C.D.Swift, R.E.Price, P.Venugopala: X-ray Fluorescence Yields, Auger, and Coster-Kronig Transition Probabilities. Rev.Mod.Phys. 44, 4 (1972) 716

/11/ S.von Goeler, W.Stodiek, N.Sauthoff: Studies of Internal Disruptions and m = 1 Oscillations in Tokamak discharges with Soft-X-ray Techniques. Phys.Rev.Letters 33, 20 (1974) 1201

/12/ A.L.Merts, R.D.Cowan, N.H.Magee: The calculated power output from a thin Iron-Seeded Plasma. LA-6220-MS, March 1976

/13/ S.von Goeler: X-ray measurements on the ST Tokamak. Proc. of the 7th Eur.Conf.on Contr.Fusion and Plasma Phys., Lausanne 1975, Vol.II, 71-80

/14/ G.J.Boxman et al.: Low and high density operation of Alcator. Proc.of the 7th Eur.Conf.on Contr.Fusion and Plasma Phys., Lausanne 1975, Vol.II, 14-23

/15/ TFR Group, presented by D.Launois: Behaviour of discharges and internal disruptions in TFR. Proc.of the 7th Eur.Conf.on Contr.Fusion and Plasma Phys., Lausanne 1975, Vol.II, 1-13

/16/ W.Lotz: Ionisierungsenergien von Atomen und Ionen der Elemente H bis Ni (2 = 28). IPP 1/49 (1966) and J.O.S.A. 57, 873 (1976)

/17/ J.L.Schwob: Potentials d'Ionisation des ions des Elements du Gallium au Molybdene. EUR-CEA-FC-720, Janvier 1974

/18/ TFR Group: Numerical Simulation of the impurity peak positions in TFR 400 discharges. EUR-CEA-FC-947, March 1978

/19/ C.Breton,C.De Michelis, M.Finkenthal: Ionisation equilibrium of selected elements from Neon to Tungsten of interest in Tokamak research. EUR-CEA-FC-948, March 1978

/20/ C.Breton, C.De Michelis, M.Mattioli: Ionisation Equilibrium and Radiation Cooling of a high temperature plasma. EUR-CEA-FC-853, Dec.1976 (Their computer program was kindly made available to us.)

/21/ H.Hacker, private communication

/22/ W.Engelhardt: Diffusion of Impurities in Pulsator Tokamak. APS meeting, Atlanta 1977

/23/ W VII-A Team: Ohmic Heating Experiments in the W VII-A Stellarator. Proc.of the 8th Eur.Conf.on Contr.Fusion and Plasma Physics, Prague 1977, Vol.II, 73-92

/24/ Equipe TFR: Oxygen Gas Injection during the current plateau of a TFR tokamak plasma. Nuclear Fusion 17, 6 (1977) 1297

/25/ S. von Goeler et al.: Soft X-ray measurements on the PLT tokamak. PPPL-1383, October 1977

/26/ M. Klapisch et al.: Identification of forbidden lines in the soft X-ray spectrum of the TFR tokamak. EUR-CEA-FC-945, January 1978

/27/ P. Smeulders: Second order Abel inversion with allowance for spatial resolution. IPP 2/240, August 1978

/28/ Equipe TFR: Internal disruptions and current breakdown in TFR. Proc. of the 6th Int. Conf. on Plasma Physics and Contr. Nucl. Fusion Research, Berchtesgaden 1976, IAEA-CN-35/A 8

/29/ W VII-Team : Energy and particle confinement in the ohmnically heated W VII-A Stellarator. Proc. of the 7th Int. Conf. on Plasma Physics and Contr. Nucl. Fusion, Innsbruck 1978.